A NOVEL FRAMEWORK FOR SOLVING TWO-DIMENSIONAL CONSOLIDATION PROBLEM USING RANDOM FEYNMAN-KAC FORMULATION

Naina Deb[1], Budhaditya Hazra[2], Arindam Dey[3]

[1]Research Scholar, Department of Civil Engineering, Indian Institute of Technology, Guwahati, Assam, India, 781039; email: nainadeb21@iitg.ac.in

[2]Associate Professor, Department of Civil Engineering, Indian Institute of Technology, Guwahati, Assam, India, 781039; email: budhaditya.hazra@iitg.ac.in

[3]Associate Professor, Department of Civil Engineering, Indian Institute of Technology, Guwahati, Assam, India, 781039; email: arindam.dey@iitg.ac.in (corresponding author)

ABSTRACT

This paper presents a novel framework for solving the plane strain two-dimensional (2D) consolidation problem of saturated soils using the random Feynman-Kac (RF-K) formulation. The proposed framework addresses the inherent spatial variability of soils by modeling the coefficients of horizontal (c_h) and vertical (c_v) consolidation as 2D random fields, generated using the Karhunen-Loeve (K-L) expansion. Stochastic differential equations (SDEs), formulated as generators corresponding to the governing partial differential equation (PDE) of the 2D consolidation problem, are used to simulate the trajectories of pore water dissipation using Monte Carlo (MC) simulations. These trajectories are simulated until the exit time (T_e) and the excess pore water pressure solutions (EPWP) are calculated by taking the expectation over the ensemble of simulated trajectories under various drainage boundary conditions with uniform initial conditions. In addition to the RF-K framework, a random field finite difference method (RF-FDM) is developed incorporating random fields of c_h and c_v. The solutions obtained using the RF-K framework are then compared

with those obtained using the proposed RF-FDM framework incorporating the same random fields of c_h and c_v. To further validate the accuracy of the RF-K framework, it is applied to the simple case of the one-dimensional (1D) consolidation problem, and resulting solutions are benchmarked against both the FDM and existing analytical solutions. The study illustrates the robustness and accuracy of the RF-K framework in different drainage boundary cases and demonstrates its potential to model consolidation processes in heterogeneous soils. Taking into account the spatial variability of soils in both 1D and 2D consolidation scenarios, the proposed approach offers a significant advancement in the probabilistic analysis of the consolidation of saturated soils.
Keywords: 2D Consolidation, Feynman-Kac formula, Random Field, Monte-Carlo simulations, Finite Difference Method, Excess Pore-Water Pressure

---

1 INTRODUCTION

The stability and settlement of the structures (buildings, bridges and dams) are significantly influenced by the consolidation of saturated soft soils, which is caused by the accumulation of excess pore-water pressure (EPWP) under applied external loads, followed by subsequent expulsion of pore-water. The classical theory of one-dimensional (1D) consolidation of saturated soils by Terzaghi [1] posits it to be a small strain phenomenology, assuming vertical dissipation of EPWP through single or double drainage while restricting any lateral deformation. Although it provides a simplified approach towards the understanding of the consolidation phenomenon, it falls short in addressing real-world complex situations due to its restrictive assumptions. In reality, pertinent geotechnical projects dealing with the settlement of embankments, dams, and foundations are influenced by the two-dimensional (2D) dissipation of pore-water, complex boundary conditions, anisotropic soil behavior, and mixed drainage conditions. Rendulic [2] extended the 1D consolidation framework to include two- and three-dimensional cases, leading to the development of the Terzaghi-Rendulic theory. This theory assumes that during consolidation under constant external loading, the total normal stresses at a given point in the soil remain unchanged. The implicit assumptions of the Terzaghi-Rendulic theory simplified the consolidation problem, transforming it into a much simpler diffusion equation.

In traditional consolidation analyses, it is assumed that the soil is homogeneous and the properties such as consolidation coefficients, permeability, and volume compressibility are deterministic and constant throughout the soil domain. However, in reality, the soil is heterogeneous [3], and these soil properties exhibit inherent spatial variability [4–7]. Neglecting spatial variability can result in significant errors in estimating EPWP and subsequent settlement. This is particularly critical for large-scale projects where heterogeneity in soil properties greatly influences the consolidation process. As a result, efficient models are necessary to accurately analyze and predict consolidation behavior under different loading scenarios and boundary conditions.

Various significant studies have focused on the development of analytical and semi-analytical methods that address different loading and boundary conditions in 2D consolidation problems [8–11]. Huang and Li [12] developed a generalized analytical solution for 2D plane strain consolidation of unsaturated soils with time-dependent drainage boundaries, analyzing the influence of drainage parameters on EPWP and excess pore air pressure dissipation. Utilizing Laplace transform and Fourier analysis, Wang et al. [13] derived semi-analytical solutions for plane strain 2D consolidation of unsaturated soils considering time- and depth-dependent stress with a multistage loading scheme. A recent study by Xie et al. [14] explored the analytical solution for the 2D consolidation of visco-elastic saturated soils under cyclic loading, specifically addressing the impact of leakage during the operation of an underground tunnel. Sun et al. [15] recently proposed semi-analytical solutions for 2D consolidation in interbedded soils incorporating clay layer interactions using Laplace transforms, Fourier analysis, and boundary transformation in the frequency domain. While analytical and semi-analytical approaches provide valuable insights, they are limited by simplified assumptions, regular domain geometries, and specific parameter constraints, highlighting the necessity of numerical methods for more complex and realistic scenarios.

Over the years, numerical methods have emerged as powerful tools for addressing the complexities of 2D consolidation problems under realistic conditions, as highlighted in several studies [16–18]. Tang et al. [19] developed finite element solutions for 1D and 2D consolidation in saturated and unsaturated soils, incorporating coupled and uncoupled analyses in both axisymmetric and plane strain cases. While numerical approaches effectively model 2D consolidation, they require extensive domain discretization, leading to high computational costs. Moreover, these techniques often operate within a deterministic framework that demands precise input data and calibration, which can be challenging. This highlights the growing need for probabilistic computational frameworks to address uncertainties and improve predictability.

Probabilistic computational approaches have seen substantial progress, with advancements in random field modeling techniques [20, 21]. Bong et al. [22] proposed new probabilistic approaches for modeling consolidation under vertical, radial, and combined drainage conditions using stochastic surface response and first-order reliability methods. Using a subset simulation approach, Houmadi et al. [23] conducted a probabilistic analysis of the 2D Biot's consolidation problem under uniform surcharge loading, taking into account Young's modulus as an anisotropic random field. Recently, solving the consolidation problem has also bolstered the usage of machine learning techniques [24–26]. Wang et al. [27] used physics-informed neural networks (PINN) for forward and inverse analysis of 2D plane strain and axisymmetric consolidation of soils from limited measurements, and the results are compared with those obtained from the finite difference method (FDM). In the physics-informed deep learning framework, Guo and Yin [28] used continuous and discrete methods to conduct forward and inverse studies of 1D, 2D, and 3D soil consolidation under different drainage boundary conditions.

Building on the growing interest in probabilistic and computational approaches for modeling the 2D consolidation of soils, one promising framework that has yet to be fully explored in geotechnical applications is the Feynman-Kac (F-K) formula [29, 30]. The F-K formula uniquely connects the solutions of governing partial differential equations (PDEs) with the expected values of functionals of a stochastic process, offering a probabilistic interpretation of deterministic problems. Since its introduction in quantum mechanics [31], it has been widely used in a variety of fields, such as engineering [32], physics [33], and financial mathematics [34]. Alghassi et al. [35] developed a quantum algorithm for solving PDEs derived from higher-dimensional stochastic differential equations (SDEs), demonstrating consistency with the forward Euler method and Monte Carlo Simulation (MCS). Recently, Hawkins et al. [36] presented a McKean-Markov branched sampling approach for solving forward-backward SDE.

Studies reveal that there are very few semi-analytical, analytical, and numerical solutions for 2D soil consolidation. The majority of current research focuses on unsaturated soil conditions or 2D axisymmetric consolidation, with limited analytical methods for plane-strain 2D consolidation in fully saturated soils. Although probabilistic and computational methods have recently gained increased attention for addressing uncertainties and complexities in the 2D soil consolidation problem, the field is still emerging with few notable contributions. Despite its proven effectiveness in other domains, the potential application of the F-K formulation in soil consolidation analysis, particularly in random field modeling of soil parameters, remains unexplored. To improve predictions of EPWP dissipation and settlement and analyze the consolidation behavior of soil from a probabilistic perspective, the F-K technique may offer a novel approach to addressing uncertainties in soil properties and boundary conditions.

The key contribution of the present work is the probabilistic solution to the 2D plane strain consolidation problem of saturated soils, based on a novel random Feynman-Kac (RF-K) formulation incorporating the spatial variability of the consolidation coefficients under various drainage boundary and uniform initial conditions. This meshless framework utilizes two SDEs as generators of stochastic processes in two spatial directions, corresponding to the governing bi-directional parabolic PDE. The coefficients of horizontal (c_h) and vertical (c_v) consolidation are modeled as random fields generated by the Karhunen-Loève (K-L) expansion technique and incorporated into the SDEs. The SDEs are simulated using MCS, and the pore-water trajectories within the consolidating domain of saturated soil are simulated using the Euler-Maruyama method within the framework of MCS of SDEs. The Brownian particles are absorbed or reflected according to the boundary conditions, and the expected value of the pore-water trajectories yields the EPWP solutions to the 2D consolidation problem. Additionally, a random field finite difference method (RF-FDM) is developed to analyze the 2D plane strain consolidation problem, incorporating the random fields of c_h and c_v. The results obtained from the RF-K framework are compared and validated against those from the RF-FDM approach.

2 MATHEMATICAL BACKGROUND

2.1 Theory of Consolidation

The classical one-dimensional (1D) consolidation theory is widely used to analyze the consolidation behavior of soils and describe the spatiotemporal behavior of excess pore water pressure (EPWP). The governing partial differential equation (PDE) of 1D consolidation of saturated and homogeneous soils, as in [37], is given by:

$$\frac{\partial u(z,t)}{\partial t} = c_v \frac{\partial^2 u(z,t)}{\partial z^2} \tag{1}$$

where, c_v represents the coefficient of consolidation and $u(z,t)$ is EPWP, which is a function of depth, z and time t. The initial condition (at $t = 0$) and boundary conditions (at $z = 0$ and at $z = L_z$) associated with the 1D consolidation PDE are given by

$$u(z,0) = u_0; \quad \frac{\partial u(0,t)}{\partial z} = 0; \quad u(L_z,t) = 0 \tag{2}$$

The boundary conditions represent single drainage along the vertical direction, where only the top boundary allows water to exit the soil domain. This condition is referred to as S_v condition, denoting single drainage in the vertical direction with a permeating top boundary, as described further in the paper. The analytical solution to the 1D consolidation Eq. (1) as in [37] is given by

$$u(z,t) = \frac{4u_0}{\pi} \sum_{m=1}^{\infty} \frac{(-1)^{m-1}}{2m-1} \cos\left[(2m-1)\frac{\pi z}{2L_z}\right] \exp\left[-(2m-1)^2 \frac{\pi^2}{4} \frac{c_v t}{L_z^2}\right] \tag{3}$$

The governing PDE of plane-strain two-dimensional (2D) consolidation of saturated soils, as in [38] is given by:

$$\frac{\partial u(x,z,t)}{\partial t} = c_h \frac{\partial^2 u(x,z,t)}{\partial x^2} + c_v \frac{\partial^2 u(x,z,t)}{\partial z^2} \tag{4}$$

where $u(x, z, t)$ is the EPWP, x and z represent the horizontal and vertical directions, respectively, t signifies time, and c_h and c_v are the coefficients of horizontal and vertical consolidation, respectively, defined by:

$$c_h = \frac{k_\mathrm{h}}{\gamma_\mathrm{w} m_\mathrm{v}}; \quad c_v = \frac{k_\mathrm{v}}{\gamma_\mathrm{w} m_\mathrm{v}} \tag{5}$$

where k_h and k_v are coefficients of horizontal and vertical permeability, respectively, γ_w is the unit weight of water, and m_v is the coefficient of volume compressibility. The initial condition of the 2D consolidation problem is given by:

$$u(x, z, 0) = u_0; \quad (t = 0) \tag{6}$$

where, u_0 signifies the uniform initial pore water pressure across the soil domain. The 2D consolidation equation Eq. (4) is subjected to boundary conditions given by:

2.1.1 $S_v S_h$ Boundary Conditions

The bottom ($z = 0$) and top ($z = L_z$) boundary conditions are as follows:

$$\frac{\partial u(x, 0, t)}{\partial z} = 0; \quad u(x, L_z, t) = 0 \tag{7}$$

The left ($x = 0$) and right ($x = L_x$) boundary conditions are as follows:

$$\frac{\partial u(0, z, t)}{\partial x} = 0; \quad u(L_x, z, t) = 0 \tag{8}$$

A pictorial representation of the $S_v S_h$ drainage boundary conditions for the 2D consolidation problem is shown in Figure 1(a). The top and right boundaries permeate and allow water drainage, whereas the bottom and left boundaries do not permeate, restricting the flow of water out of the soil domain.

2.1.2 $D_v S_h$ Boundary Conditions

The bottom ($z = 0$) and top ($z = L_z$) boundary conditions are as follows:

$$u(x, 0, t) = 0; \quad u(x, L_z, t) = 0 \tag{9}$$

The left ($x = 0$) and right ($x = L_x$) boundary conditions are as follows:

$$\frac{\partial u(0, z, t)}{\partial x} = 0; \quad u(L_x, z, t) = 0 \tag{10}$$

For $D_v S_h$ drainage boundary conditions, as shown in Figure 1(b), in addition to the permeating top and right boundaries, drainage of water is also allowed through the permeating bottom boundary, whereas the non-permeating left boundary restricts the flow of water out of the soil domain.

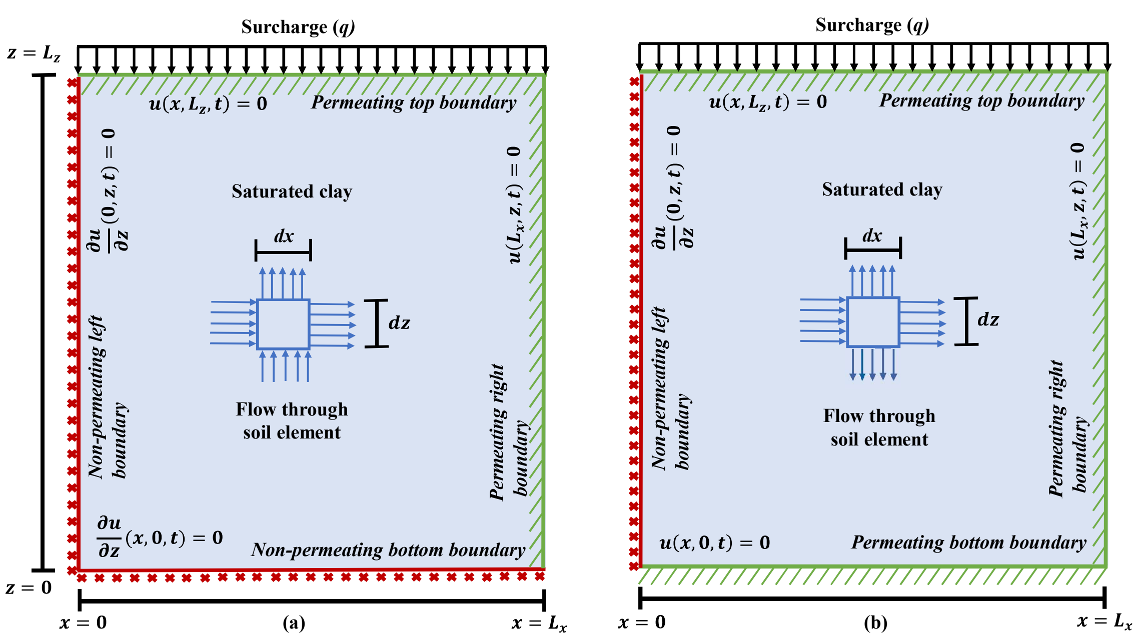

Figure 1: Schematic illustration of 2D consolidation problem under (a) $S_v S_h$ drainage (b) $D_v S_h$ drainage conditions.

2.2 The Feynman-Kac (F-K) Formula: An Overview

The F-K formula offers a probabilistic method for solving specific PDEs by connecting them with stochastic processes, particularly Brownian motion [30]. It establishes a relationship between the solutions of parabolic and elliptic PDEs and the expected values of functionals derived from stochastic processes. For a generalized PDE of the form as in [39] given by

$$\frac{\partial w(y,t)}{\partial t} + a(y)\frac{\partial w(y,t)}{\partial y} + \frac{1}{2}b^2(y)\frac{\partial^2 w(y,t)}{\partial y^2} - cw(y,t) = 0 \tag{11}$$

with the condition:

$$w(y,T) = \phi(y) \tag{12}$$

where, $w(y,t)$ is the unknown function to be solved, $a(y)$, $b(y)$, and $\phi(y)$ are some known functions, and c is a positive constant. $w(y,T) = \phi(y)$ is the terminal condition of the problem at $t = T$. Eq. (11) takes a form similar to a backward Kolmogorov equation, which can be addressed through the F-K formula. To solve the PDE as in Eq. (11) with the F-K formula, it needs to be converted to a stochastic differential equation (SDE) having drift and diffusion terms.

Define a stochastic process y_t having drift and diffusion terms that correspond to the PDE as in Eq. (11) given by:

$$dy_t = a(y)dt + b(y)dB_t \tag{13}$$

where, $a(y)$ and $b(y)$ represent the SDE's drift and diffusion terms, respectively, and B_t signifies the Brownian motion. According to the F-K formula, the solution $w(y,t)$ to the PDE can be expressed as the expected value of a functional related to the stochastic process y_t. With the terminal condition as in Eq. (12), the solution $w(y,t)$ as in [39] can be represented as follows:

$$w(y,t) = \mathbb{E}\left[\exp\left(-\int_t^T c(y_s,s)\,ds\right)\phi(y_T) \mid y_t = y\right] \tag{14}$$

where, $\exp\left(-\int_t^T c(y_s,s)\,ds\right)$ accounts for the term $cw(y,t)$ in the PDE, and $\phi(y_T)$ is the terminal value of $w(y,T)$ at T, based on the stochastic process y_t. Eq. (14) represents the F-K formula, which gives a solution to the generalized PDE as in Eq. (11).

2.3 Karhunen-Loève (K-L) Expansion for Random Fields

A *random field* is a collection of random variables indexed by points in space [40]. For a domain $D \subset \mathbb{R}^d$, a random field $v(y,\omega)$ is defined such that $v(y,\omega)$ is a random variable for each point $y \in D$ and for each outcome ω in a probability space Ω [41]. In mathematical terms, a random field satisfies $(v(y,\omega) \in L^2(\Omega, L^2(D)))$ as in [42], which implies that:

$$\mathbb{E}\left[\int_D |v(y,\omega)|^2\,dy\right] < \infty$$

This ensures the random field has well-defined statistical properties, such as mean and covariance, which are essential for its mathematical and physical interpretations. The covariance function $\mathbb{C}(y,x)$ of a random field $v(y,\omega)$ as in [42] is defined as:

$$\mathbb{C}(y,x) = \mathbb{E}\left[(v(y,\omega) - \mu(y))(v(x,\omega) - \mu(x))\right] \tag{15}$$

where, $\mu(y) = \mathbb{E}[v(y,\omega)]$ is the mean value of the random field. The covariance operator $\mathbb{C}$ associated with the covariance function acts on functions $\Phi(x)$ defined over D as in [42] is given by:

$$(\mathbb{C}\Phi)(y) = \int_D \mathbb{C}(y,x)\Phi(x)\,dy \tag{16}$$

The operator in Eq. (16) is central to the Karhunen-Loève (K-L) expansion, as its eigenfunctions and eigenvalues provide the orthonormal basis and weights for the expansion.

The *K-L expansion* is an essential mathematical technique employed for expressing a random field using orthogonal functions and uncorrelated random variables. It efficiently models spatial variability in stochastic processes by characterizing and simulating the uncertainty of soil properties, material variability, and environmental factors. For a random field $v(y,\omega)$ with mean $\mu(y)$, the K-L expansion representation of the random field as in [42] is given as:

$$v\,(y,\omega) = \mu(y) + \sum_{i=1}^{\infty} \sqrt{\lambda_i}\Phi_i(y)\xi_i(\omega) \tag{17}$$

where $\{\lambda_i\}$ are the eigenvalues of the covariance operator $\mathbb{C}$ of the random field such that $\lambda_1 \geq \lambda_2 \geq \cdots \geq 0$, $\{\Phi_i\}$ are the eigenfunctions, forming an orthonormal basis for the space $L^2(D)$, and $\xi_i(\omega)$ are uncorrelated standard normal random variables such that $\mathbb{E}[\xi_i(\omega)] = 0$, $\mathbb{E}[\xi_i^2(\omega)] = 1$ and $\mathbb{E}[\xi_i(\omega)\xi_j(\omega)] = \delta_{ij}$. The random variables $\xi_i(\omega)$ are defined by the projection of the deviation of the random field from its mean onto each eigenfunction as in [42] as follows:

$$\xi_i(\omega) := \frac{1}{\sqrt{\lambda_i}}\langle v(y,\omega) - \mu(y), \Phi_i(y)\rangle_{L^2(D)} \tag{18}$$

The inner product $\langle\cdot,\cdot\rangle_{L^2(D)}$ in the L^2 space defined in D quantifies how well the eigenfunction Φ_i captures the variation in the random field $v(y,\omega)$. In practical applications, a truncated K-L expansion is often employed to approximate the random field by keeping only the first K terms, thus reducing computational demands while capturing the dominant variability modes, particularly when eigenvalues decay quickly. The truncated K-L expansion [42] of a random field is given by:

$$v_K\,(y,\omega) := \mu(y) + \sum_{i=1}^{K} \sqrt{\lambda_i}\Phi_i(y)\xi_i(\omega) \tag{19}$$

where $v_K(y, \omega)$ is a random field with mean $\mu(y)$. The K-L expansion effectively represents the mean and spatial variability of a domain, provides an understanding of the spatial correlation structure, enables efficient computation by truncating the series to keep only the key modes, and simplifies the simulations of complex random fields.

3 PROPOSED FORMULATIONS

3.1 Numerical Solutions Using the Finite Difference Method

To solve the governing 2D consolidation Eq. (4) using the Finite Difference Method (FDM), the spatial domain is divided into a grid with spacing Δx and Δz along the x and z axes, respectively, and the time domain is discretized with a time step Δt. Numerical solutions to the 2D plane strain consolidation Eq. (4) will be derived using two approaches: one using the deterministic finite difference method (DFDM), where c_h and c_v are considered constant parameters, and the other using the random field finite difference method (RF-FDM), where c_h and c_v are considered as random fields.

3.1.1 Deterministic Finite Difference Method (DFDM)

Let $u^n_{i,j}$ represent the EPWP at grid point (i, j) at time step n. For the partial second-order derivatives in Eq. (7), using central difference approximation gives,

$$\frac{\partial^2 u}{\partial x^2} \approx \frac{u^n_{i+1,j} - 2u^n_{i,j} + u^n_{i-1,j}}{\Delta x^2} \tag{20}$$

$$\frac{\partial^2 u}{\partial z^2} \approx \frac{u^n_{i,j+1} - 2u^n_{i,j} + u^n_{i,j-1}}{\Delta z^2} \tag{21}$$

For the first-order time derivative of Eq. (7), using the forward difference scheme gives,

$$\frac{\partial u}{\partial t} \approx \frac{u^{n+1}_{i,j} - u^n_{i,j}}{\Delta t} \tag{22}$$

Substituting the approximations of Eq. (20) – Eq. (22) into Eq. (7) yields,

$$u_{i,j}^{n+1} = u_{i,j}^{n} + \Delta t \left(c_h \frac{u_{i+1,j}^{n} - 2u_{i,j}^{n} + u_{i-1,j}^{n}}{\Delta x^2} + c_v \frac{u_{i,j+1}^{n} - 2u_{i,j}^{n} + u_{i,j-1}^{n}}{\Delta z^2} \right) \tag{23}$$

The solution $u(x, z, t)$ of the 2D consolidation equation (7) can be obtained by iteratively solving Eq. (23) for each time step. To ensure the stability of solutions during the time marching process for explicit schemes, the time step must satisfy the criterion given by:

$$\Delta t \leq \frac{1}{2} \left(\frac{\Delta x^2}{c_h} + \frac{\Delta z^2}{c_v} \right) \tag{24}$$

The solution in Eq. 23 gives the DFDM solution to the 2D plane strain consolidation Eq. (7) where c_h and c_v are constants. To obtain a random field finite difference solution, the spatial variability of c_h and c_v must be incorporated in the finite difference scheme as in Eq. (23).

3.1.2 Random Field Finite Difference Method (RF-FDM)

For the RF-FDM approach, the spatial variability of c_h and c_v are incorporated into the finite difference scheme as given in Eq. (23). If c_h and c_v are considered as random fields generated by Karhunen-Loève (K-L) expansion following Eq. (47), it can be written as:

$$c_h(x, z, \omega) = \overline{c_h(x, z)} + \sum_{k=1}^{N} \sqrt{\lambda_k^h}\ \phi_k(x, z)\ \xi_k(\omega) \tag{25}$$

$$c_v(x, z, \omega) = \overline{c_v(x, z)} + \sum_{k=1}^{N} \sqrt{\lambda_k^v}\ \psi_k(x, z)\ \eta_k(\omega) \tag{26}$$

where $\overline{c_h}$ and $\overline{c_v}$ are the mean values of c_h and c_v, respectively; λ_k^h and λ_k^v are the eigenvalues of the respective covariance matrices; $\phi_k(x, z)$ and $\psi_k(x, z)$ are the eigenfunctions; $\xi_k(\omega)$ and $\eta_k(\omega)$ are independent Gaussian random variables. N is the number of terms retained in the expansion.

Incorporating Eq. (25)-Eq. (26) into the finite difference scheme as in Eq. (23) gives,

$$\begin{aligned} u_{i,j}^{n+1} = u_{i,j}^{n} &+ \Delta t\left[\left\{\overline{c_h(x,z)} + \sum_{k=1}^{N} \sqrt{\lambda_{h_k}}\phi_k(x,z)\xi_k(\omega)\right\}\frac{u_{i+1,j}^{n} - 2u_{i,j}^{n} + u_{i-1,j}^{n}}{\Delta x^2}\right] \\ &+ \Delta t\left[\left\{\overline{c_v(x,z)} + \sum_{k=1}^{N} \sqrt{\lambda_{v_k}}\psi_k(x,z)\eta_k(\omega)\right\}\frac{u_{i,j+1}^{n} - 2u_{i,j}^{n} + u_{i,j-1}^{n}}{\Delta z^2}\right] \end{aligned} \tag{27}$$

Eq. (27) represents the finite difference scheme to the 2D consolidation Eq. (7) obtained using RF-FDM implementing random fields of c_h and c_v. Solving Eq. (27) iteratively for each time step gives the solution $u(x, z, t, \omega)$ using the RF-FDM approach.

3.2 Proposed Formulation: Random Feynman-Kac (RF-K) Framework

The 2D consolidation Eq. (7) is a forward parabolic PDE of diffusion type, governing the excess pore water pressure $u(x, z, t)$ within a porous medium. The F-K formula connects the solution of the backward parabolic PDE, corresponding to the forward PDE, to the expected value of a function for a stochastic process that progresses backward in time.

The backward PDE of the 2D consolidation Eq. (7) describing how the solution evolves backward in time from a terminal condition at some exit time T_e is given by:

$$\frac{-\partial u(x,z,t)}{\partial t} = \frac{1}{2}\left(\sqrt{2c_h}\right)^2\frac{\partial^2 u(x,z,t)}{\partial x^2} + \frac{1}{2}\left(\sqrt{2c_v}\right)^2\frac{\partial^2 u(x,z,t)}{\partial z^2} \tag{28}$$

subjected to the terminal condition given by:

$$u\left(x, z, T_e\right) = \zeta\left(x, z\right) \tag{29}$$

where T_e represents the exit time. The negative sign in the time derivative in Eq. (28) represents that it evolves backward in time. The second-order spatial derivatives remain the same as in the forward partial differential Eq. (7). The F-K formula gives a probabilistic interpretation of the solution $u(x, z, t)$ of the backward PDE (28) as the expected value of a function of a stochastic process that solves the corresponding SDE.

The application of the F-K formula to the backward PDE in Eq. (28) relies on linking the second-order spatial derivatives in x and z to Brownian motion. These second-order derivatives ($\partial^2 u/\partial x^2$ and $\partial^2 u/\partial z^2$) in the PDE imply that the spatial variables follow stochastic processes. Let $B_x(t)$ and $B_z(t)$ be two independent Brownian motions representing the randomness in the horizontal and vertical directions. For the backward 2D consolidation PDE (28), the corresponding SDEs that describe the motion of particles evolving in horizontal and vertical directions, respectively, are given by:

$$dX_t = \sqrt{2c_h} dB_x(t) \tag{30}$$

$$dZ_t = \sqrt{2c_v} dB_z(t) \tag{31}$$

where X_t and Z_t are the positions of the Brownian particles at time t in the horizontal and vertical directions, respectively. Eq. (30) and Eq. (31) are the two zero drift SDEs corresponding to the 2D consolidation Eq. (28) having diffusion terms as $\sqrt{2c_h}$ and $\sqrt{2c_v}$, respectively. These two SDEs describe how the particles diffuse randomly over time, with diffusion controlled by the consolidation coefficients, c_h and c_v. Using Ito's lemma and Taylor series expansion for $u(x, z, t)$ gives,

$$\begin{aligned} du(x, z, t) = \frac{\partial u(x, z, t)}{\partial t} dt + \frac{\partial u(x, z, t)}{\partial x} dx_t + \frac{1}{2} \frac{\partial^2 u(x, z, t)}{\partial x^2} (dx_t)^2 \\ + \frac{\partial u(x, z, t)}{\partial z} dz_t + \frac{1}{2} \frac{\partial^2 u(x, z, t)}{\partial z^2} (dz_t)^2 \end{aligned} \tag{32}$$

Substituting Eq. (29) and Eq. (30) in Eq. (31) and further simplifying and recalling the properties of quadratic variation [39] results in

$$\begin{aligned} du(x,z,t) &= \frac{\partial u(x,z,t)}{\partial t}dt + \frac{\partial u(x,z,t)}{\partial x}\left(\sqrt{2c_h}\right)dB_x(t) + \frac{1}{2}\frac{\partial^2 u(x,z,t)}{\partial x^2}\left(\sqrt{2c_h}dB_x(t)\right)^2 \\ &+ \frac{\partial u(x,z,t)}{\partial z}\left(\sqrt{2c_v}\right)dB_z(t) + \frac{1}{2}\frac{\partial^2 u(x,z,t)}{\partial z^2}\left(\sqrt{2c_v}dB_z(t)\right)^2 \\ &= \left(\frac{\partial u(x,z,t)}{\partial t} + c_h\frac{\partial^2 u(x,z,t)}{\partial x^2} + c_v\frac{\partial^2 u(x,z,t)}{\partial z^2}\right)dt + \left(\sqrt{2c_h}\right)\frac{\partial u(x,z,t)}{\partial x}dB_x(t) \\ &+ \left(\sqrt{2c_v}\right)\frac{\partial u(x,z,t)}{\partial z}dB_z(t) \end{aligned} \tag{33}$$

The backward PDE of the 2D consolidation equation, as in Eq. (28) yields;

$$\left(\frac{\partial u(x,z,t)}{\partial t} + c_h\frac{\partial^2 u(x,z,t)}{\partial x^2} + c_v\frac{\partial^2 u(x,z,t)}{\partial z^2}\right) = 0 \tag{34}$$

Substituting Eq. (34) in Eq. (33) results in;

$$du(x,z,t) = \left(\sqrt{2c_h}\right)\frac{\partial u(x,z,t)}{\partial x}dB_x(t) + \left(\sqrt{2c_v}\right)\frac{\partial u(x,z,t)}{\partial z}dB_z(t) \tag{35}$$

Integrating Eq. (35) from t to T_e and substituting terminal conditions yields;

$$\begin{aligned} \zeta(x(T_e), z(T_e)) - u(x,z,t) &= \int_t^{T_e} \frac{\partial u(x,z,t)}{\partial x}\left(\sqrt{2c_h}\right)dB_x(t) \\ &+ \int_t^{T_e} \frac{\partial u(x,z,t)}{\partial z}\left(\sqrt{2c_v}\right)dB_z(t) \end{aligned} \tag{36}$$

Upon taking expectations on both sides of Eq. (36), conditioned on $X_t = x$ and $Z_t = z$, and observing that the right-hand side is an Ito integral whose expectation is zero, which after further rearranging leads to,

$$u(x,z,t) = E\left[\zeta(x(T_e), z(T_e))\,|X_t = x, Z_t = z\right] \tag{37}$$

where, $(x(T_e), z(T_e))$ represents the position of the water particles at the exit time T_e according to the SDEs. The deterministic Feynman-Kac (DF-K) formula in Eq. (37) expresses the solution to the 2D consolidation equation at any point $u(x,z,t)$. This is achieved by initiating the stochastic processes in Eqs. (30) and (31) from (x, z) at time t and evolving them until the exit time T_e. The solution is given by the expected value of $\zeta(z(T_e), z(T_e))$, conditioned on the initial positions $(X_t = x, Z_t = z)$, across multiple realizations of the stochastic processes. The DF-K formula thus propagates the final condition $\zeta(z(T_e), z(T_e))$ backward in time to determine the solution at $u(x, z, t)$.

Incorporating the spatial variability of c_h and c_v into the F-K framework by modeling c_h and c_v as random fields, the solution to the 2D consolidation equation becomes the expected value over both the stochastic processes and the random fields. The solution $u(x, z, t)$ is given by:

$$u(x, z, t) = E_{\xi,\eta}\left[E[\zeta(x(T_e), z(T_e)) \mid X_t = x, Z_t = z]\right] \tag{38}$$

The inner expectation $E[\zeta(x(T_e), z(T_e)) \mid X_t = x, Z_t = z]$ is calculated over the trajectories of water particles governed by the stochastic differential equations presented in Eqs. (30) and (31). Meanwhile, the outer expectation, $E_{\xi,\eta}$, is evaluated over the random fields of c_h and c_v, which depend on the independent random variables, ζ and η derived from the K-L expansion of c_h and c_v as defined in Eqs. (25) and (26). Eq. (38) gives the random Feynman-Kac (RF-K) solutions to the 2D consolidation Eq. (4), where the spatial variability is incorporated by modeling c_h and c_v as random fields.

4 IMPLEMENTATION AND SIMULATION FRAMEWORK

4.1 Generation of Random Fields of c_h and c_v

For implementation in the RF-K and RF-FDM frameworks, 2D random fields of c_h and c_v are generated using K-L expansion as in Eq. (25)-Eq. (26). The autocovariance function commonly used in geotechnical engineering studies for modeling spatial variability is exponential [21] given by:

$$\mathbb{C}(x_1, x_2) = \exp\left(-\frac{|x_1 - x_2|}{l}\right) \tag{39}$$

where l represents the correlation distance. The random fields of c_h and c_v will be spatially autocorrelated following the autocovariance function as in Eq. (39). As the spatial variability is in both x and z directions in the 2D consolidation problem, an anisotropic exponential covariance function as in [21] is used for modeling the 2D spatial variability of random fields for c_h and c_v given by:

$$\mathbb{C}(x, z) = \exp\left(-\frac{|x_1 - x_2|}{l_h} - \frac{|z_1 - z_2|}{l_v}\right) \tag{40}$$

where l_h and l_v are the horizontal and vertical correlation distances, respectively. Eq. (40) ensures that the covariance between two points decreases with increasing distance, wherein the decay rate is controlled by l_h and l_v. For many soil properties, horizontal correlation distances are generally estimated to range from 2 to 60 m, while vertical correlation distances are typically in the range of 1 to 6 m [5, 22, 43].

The generation of random fields for c_h and c_v within a specific range of values is essential, as their variation depends significantly on soil type, highlighting the importance of careful modeling to ensure realistic and meaningful results. For Singapore marine clay, it is reported that the value of c_h generally increases with depth and is typically 2-3 times the value of c_v, which ranges between 0.5–2 m^2/yr [44]. Consequently, following this range of c_v, the random field of c_h is generated in the range of 1.5 to 6 m^2/yr. 2D random fields of c_h and c_v are generated for various l_h and l_v using the K-L expansion, considering c_h and c_v to be spatially varying fields as shown in Figure 2. Figures 2(a)–Figure 2(c) depict the 2D random field realizations of c_h, while Figures 2(d)–Figure 2(f) show those of c_v for the same l_h and l_v.

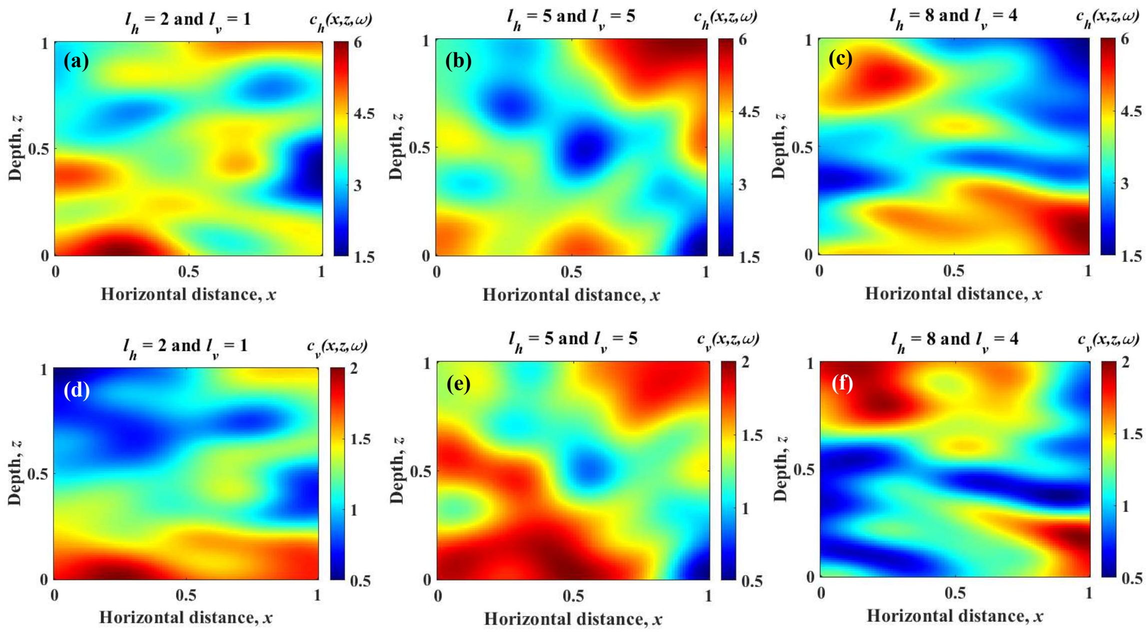

Figure 2: 2D realizations of random fields of $c_h(x, z, \omega)$ and $c_v(x, z, \omega)$ for various l_h and l_v.

The spatial domain is divided into a grid of $n_x \times n_z$ points, resulting in a total of $n = n_x \times n_z$ grid points. The covariance matrix is formed by calculating the covariance function, as in Eq. (40), across all grid points. Eigenvalue decomposition (EVD) is performed on this matrix to obtain its eigenvalues and eigenvectors. For each realization of the random fields c_h and c_v, the random variables ξ and η are sampled, and the random field is generated as described in Eqs. (25) and (26). Although c_h and c_v exhibit different patterns of variation, they are positively correlated [22].

The random fields generated for c_h and c_v are scaled so that their values fall within their specified limits using:

$$c_h^{\text{scaled}}(x, z, \omega) = c_h^{\min} + \frac{c_h(x, z, \omega) - c_h^{\min}}{c_h^{\max} - c_h^{\min}} \cdot \left(c_h^{\max} - c_h^{\min}\right) \tag{41}$$

$$c_v^{\text{scaled}}(x, z, \omega) = c_v^{\min} + \frac{c_v(x, z, \omega) - c_v^{\min}}{c_v^{\max} - c_v^{\min}} \cdot \left(c_v^{\max} - c_v^{\min}\right) \tag{42}$$

where, $c_h^{\min} = 1.5\,\mathrm{m}^2/\mathrm{yr}$, $c_h^{\max} = 6\,\mathrm{m}^2/\mathrm{yr}$, $c_v^{\min} = 0.5\,\mathrm{m}^2/\mathrm{yr}$, and $c_v^{\max} = 2\,\mathrm{m}^2/\mathrm{yr}$. The scaling of the random fields is essential, as in practical cases, c_h and c_v are constrained to lie within specific bounds due to material properties, environmental conditions, or experimental measurements.

4.2 Implementation of Random Fields of c_h and c_v into the F-K and FDM Framework

The random fields of c_h and c_v are incorporated into the FDM and F-K frameworks based on the formulations outlined in subsections 3.1 and 3.2, respectively. Following the generation of random fields for c_h and c_v using the Karhunen-Loève (K-L) expansion, these fields are integrated into the FDM and F-K frameworks, resulting in the RF-FDM and RF-K frameworks.

4.2.1 Working of the RF-K framework

The RF-K framework solves the plane-strain 2D consolidation PDE by transforming them into SDEs as in Eq. (30) and Eq. (31) and incorporating random fields by replacing the constant coefficients in the generator SDEs, making the stochastic processes location-dependent. This approach utilizes MCS to compute the solution as an expected value of the stochastic process. The framework enables modeling the dissipation of EPWP over time and space, integrating spatial variability in soil properties in the form of random fields of c_h and c_v.

Following the generation of random fields of c_h and c_v using K-L expansion as in Eq. (25) and Eq. (26), the computation domain is discretized into grid points. A set of Brownian particles is initiated at each grid point with positions corresponding to the spatial coordinates of the grid. For each particle, stochastic trajectories of EPWP are simulated over time using the Euler-Maruyama method as:

$$X_{t+\Delta t} = X_t + \sqrt{2c_h(X_t, \omega)}\Delta B_x(t) \tag{43}$$

$$Z_{t+\Delta t} = Z_t + \sqrt{2c_v(Z_t, \omega)}\Delta B_z(t) \tag{44}$$

where, Δt represents the time step of the stochastic processes, and $\Delta B_x(t)$, $\Delta B_z(t)$ represent the Brownian increments. Based on the boundary conditions, particles are either absorbed (exit the domain) or reflected (change direction) to ensure the correct physical representation of the EPWP dissipation. For S_vS_h drainage boundary conditions, as described in Eq. (7) and Eq. (8), Dirichlet boundary conditions ($u = 0$) are applied at the top and right boundaries, whereas Neumann boundary conditions ($\partial u/\partial x = 0$, $\partial u/\partial z = 0$) are imposed at the bottom and left boundaries. In contrast, for D_vS_h drainage boundary conditions, as given in Eq. (9) and Eq. (10), the top, bottom, and right boundaries are treated as Dirichlet boundaries, while a Neumann boundary condition governs the left boundary.

When the particles reach a Dirichlet boundary, it acts as an absorbent boundary, allowing the particles to exit the domain. The exit time and position of the particle are recorded, and the particle's trajectory is terminated. This approach enables pore water drainage at a Dirichlet boundary in the stochastic simulation by allowing the particles to exit the domain. In contrast, Neumann boundaries impose reflecting conditions to enforce no-flux constraints. When a particle reaches a Neumann boundary, its direction of movement is reversed, reflecting the particle back into the domain while preserving the stochastic component. This ensures that pore water drainage is restricted at the Neumann boundary in the stochastic simulation.

MCS is used to estimate the solution as an expected value over the stochastic processes and random fields following Eq. (38) by estimating the double expectation operator. The terminal condition $\zeta(x(T_e), z(T_e))$ of Eq. (38) represents the initial condition of the forward 2D plane strain

PDE because the backward PDE is solved in reverse time. In other words, when solving the backward equation as in Eq. (28), the time t progresses backward to $t = 0$, ensuring the terminal condition at the final time T_e matches with the initial condition (Eq. (9)) of the forward PDE as in Eq. (7). This reflects how the backward PDE traces the solution trajectory of the forward PDE in reverse. Hence, the expectation over the terminal condition in Eq. (38) can be written in reference to the forward PDE as:

$$E_{\xi,\eta}\left[E[\zeta(x(T_e), z(T_e)) \mid X_t = x, Z_t = z]\right] \approx E_{\xi,\eta}\left[E[u_0(x(T_e), z(T_e)) \,|X_t = x, Z_t = z]\right] \tag{45}$$

The generation of random fields c_h and c_v using K-L expansion gives N_r different realizations of the random fields. For each realization of the random fields, the particle trajectories are simulated using the Euler-Maruyama scheme as in Eq. (43) and Eq. (44). N_p independent particle simulations are run for each realization of random fields to approximate the inner expectation over the trajectories. So, for each random field realization, the solution is estimated as:

$$u^r(x, z, t) \approx \frac{1}{N_p} \sum_{i=1}^{N_p} u_o(x(T_{ei}), z(T_{ei})) \tag{46}$$

where r represents the realization of random fields and T_{ei} is the exit time of the $i-$th particle. Finally, the results from all N_r random field realizations are averaged to approximate the outer expectation. The final solution, by averaging the results in the simulation, is given by:

$$u(x, z, t) \approx \frac{1}{N_r} \sum_{r=1}^{N_r} u^r(x, z, t) = \frac{1}{N_r} \sum_{r=1}^{N_r} \left(\frac{1}{N_p} \sum_{i=1}^{N_p} u_o(x(T_{ei}), z(T_{ei})) \right) \tag{47}$$

Eq. (47) represents the final solution of the plane strain 2D consolidation problem in terms of the simulation framework. A detailed algorithm of the RF-K framework is outlined in Algorithm 1.

Algorithm 1: Feynman-Kac Framework for 2D Consolidation with Random Fields

Input: Mean values $\bar{c}_h$, $\bar{c}_v$, covariance parameters l_h, l_v, initial condition $u_0(x,z)$, boundary conditions, N_p particles, time step Δt, total time T, domain $[0, L_x] \times [0, L_z]$, number of realizations N_r.

Output: EPWP field $u(x,z,t)$ over time and space.

Step 1: Generate Random Fields for c_h and c_v

Generate N_r realizations of $c_h(x,z,\omega)$ and $c_v(x,z,\omega)$ using Eq. (25), Eq. (26).

Step 2: Initialize

Discretize domain and initialize N_p particles at each grid point (x,z).

Set the initial condition $u_0(x,z)$.

Step 3: Simulate Particle Trajectories for N_r Realizations

for $r = 1$ *to* N_r **do**

- Update particle positions using Eq. (43) and Eq. (44) based on SDEs as in Eq. (30) and Eq. (31).
- **Boundary Conditions:**
- **if** *Dirichlet condition* $u = 0$ **then**
  - Allow the water particles to exit the domain.
- **if** *Neumann condition* $\partial u/\partial x = 0$ *or* $\partial u/\partial z = 0$ **then**
  - Reflect the water particle back into the domain.

Step 4: Compute EPWP Using F-K Formula

For each grid point (x,z), compute expected value of EPWP over all N_p particles using Eq. (46).

Approximate and average over N_r realizations using Eq. (47).

Step 5: Time Evolution

for $t_k = k\Delta t$ *until* T_e **do**

- Repeat Steps 3 and 4 for each time step t_k.

Step 6: Results Visualization

Plot variation of EPWP with depth, time, and horizontal distance.

4.2.2 Working of the RF-FDM framework

The RF-FDM framework is a numerical framework that solves the plane-strain 2D consolidation PDE as in Eq. (7) with c_h and c_v modeled as random fields using K-L expansion. The solution for EPWP, $u(x.z.t)$ is obtained by solving the governing finite difference equation given by Eq. (27)

that incorporates the random fields of c_h and c_v directly into the discretization. For each realization of the random fields, a deterministic finite difference solution is computed. These individual solutions are then averaged across all realizations to determine the final EPWP distribution.

Algorithm 2: RF-FDM Scheme for 2D Consolidation

Input: L_x, L_z, N_x, N_z, Δt, T, u_0, Mean values $\bar{c}_h$, $\bar{c}_v$, covariance parameters l_h, l_v, number of K-L terms N_k, boundary conditions

Output: EPWP field, $u(x, z, t)$ over space and time

Step 1: Discretization and Initialization;
Compute $\Delta x = \frac{L_x}{N_x - 1}$, $\Delta z = \frac{L_z}{N_z - 1}$, $N_t = \frac{T}{\Delta t}$;
Initialize $u(x, z, t = 0) = u_0$;
Set the number of realizations R;
Step 2: Generate Random Fields for c_h **and** c_v;
Generate R realizations of $c_h(x, z, \omega)$ and $c_v(x, z, \omega)$ using Eq. (25), Eq. (26) ;
Verify stability criteria as in Eq. (24);
Step 3: Solve FDM for Each Realization;
for $r \leftarrow 1$ **to** R **do**
    for $n \leftarrow 1$ **to** N_t **do**
        for $i \leftarrow 2$ **to** $N_x - 1$ **do**
            for $j \leftarrow 2$ **to** $N_z - 1$ **do**
                Update u using Eq. (27);
        Apply boundary conditions for each realization;
    Store $u(x, z, t)$ for realization r;
Step 4: Post-processing of Results;
Store $u(x, z, t)$ for visualization;

The time-stepping procedure ensures that the stability condition as in Eq. (24) is satisfied for each realization to compute a stable solution of EPWP. Through this process, the framework captures the influence of spatial variability in consolidation parameters, producing EPWP distributions over time and space for each realization. A detailed algorithm for the computation of EPWP using the RF-FDM framework is given in Algorithm 2.

4.3 Validation and Comparison of the Proposed Solutions

The DFDM solutions and the DF-K solutions, where c_h and c_v are considered deterministic values for the 2D consolidation problem, have been validated against the FDM results presented by Wang et al. [27]. In their study, Wang et al. conducted FDM analyses of the plane-strain 2D consolidation problem to validate solutions obtained using PINN. Their computational domain was defined by three variables $(x, z, t) \in [0, 4] \times [0, 4] \times [0, 1]$, based on the 2D consolidation equation Eq. (7). Deterministic values of $c_h = 0.6\,\mathrm{m}^2/\mathrm{yr}$ and $c_v = 1.0\,\mathrm{m}^2/\mathrm{yr}$ were adopted, and 2D colormaps of the FDM solutions were generated for $t = 0.3$ yr and $t = 1.0$ yr.

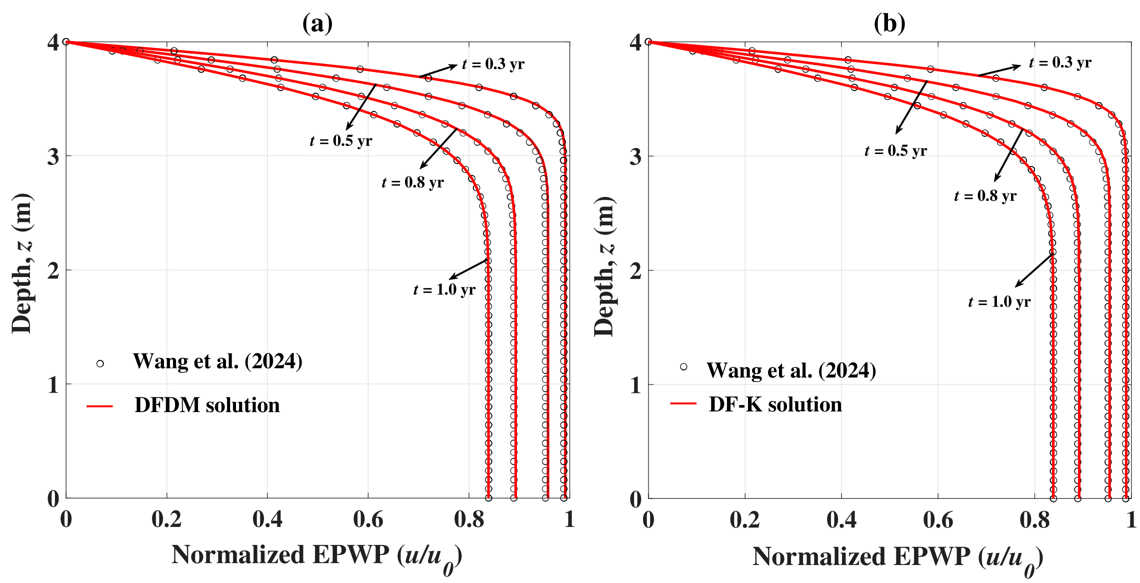

Figure 3: Comparison of the variation of EPWP profiles with depth obtained using the proposed (a) DFDM and (b) DF-K framework with the existing solution of literature.

In this study, DFDM solutions are obtained using the same domain and parameter values. The EPWP profiles from the DFDM solutions are compared with the FDM profiles by Wang et al. [27]

at a horizontal distance $x = 2\,\mathrm{m}$ and at various time intervals, as illustrated in Figure 3(a). The DFDM profiles closely match the FDM profiles, demonstrating strong agreement. Furthermore, considering c_h and c_v as 0.6 m^2/yr and 1.0 m^2/yr respectively, the EPWP profiles obtained using the proposed DF-K framework, based on Eq. (37), are compared with the FDM profiles of Wang et al. [27], as illustrated in Figure 3(b). This comparison confirms the accuracy of the proposed DF-K framework, with the DF-K and FDM profiles overlapping to a significant degree.

5 RESULTS AND DISCUSSIONS

Using the RF-K framework, the EPWP solutions for the 2D consolidation are first analyzed for both S_vS_h and D_vS_h drainage boundary conditions, as in Eqns. (7) to (10). Random fields of c_h and c_v are generated in the range of 1.5-6 m^2/yr and 0.5-2 m^2/yr, respectively, as mentioned in Subsection 4.1, using the K-L expansion expressions given by Eq. (25) and Eq. (26). For each drainage case, the evolution of EPWP with depth, horizontal distance, and time is examined to assess the dissipation patterns under uniform initial pore water pressure conditions. To validate the accuracy of the RF-K framework, the results obtained using the RF-K framework are compared with those obtained using the RF-FDM framework, where the same random fields of c_h and c_v are incorporated.

Additionally, the RF-K framework is applied to the simpler case of consolidation in one dimension (1D) to validate the robustness of the framework. In that case, only the coefficient of vertical consolidation c_v is modeled as a 1D random field to incorporate the spatial variability. The results of EPWP obtained are then compared with RF-FDM for the 1D case as well as with analytical solutions available in the literature. The following subsections present a detailed discussion of the EPWP profiles, focusing on the differences observed under S_vS_h and D_vS_h drainage cases and their implications on consolidation behavior.

5.1 Case 1: 2D Consolidation under S_vS_h Drainage

Considering the S_vS_h drainage boundary conditions given in Eq. (7) and Eq. (8), solutions of the 2D consolidation (Eq. (4)) are obtained by implementing the RF-K framework. Random fields of c_h and c_v are generated using Eq. (25) and Eq. (26) respectively, considering $l_h = 3$ and $l_v = 2$ in the covariance function, and scaled to the desired range using Eq. (41) and Eq. (42), respectively. A depth of 6 m, a horizontal distance of 6 m, and a time of 1 yr are considered for obtaining solutions of the EPWP profiles under S_vS_h drainage boundary conditions using the proposed RF-K framework. 1000 MCS are used to simulate the trajectories of EPWP employing the Euler-Maruyama scheme following the SDEs given by Eq. (30) and Eq. (31). The EPWP is normalized with respect to the uniform initial pore water pressure, u_0; the depth is normalized with respect to the total domain depth L_z, and the horizontal distance is normalized with respect to the total domain horizontal length, L_x.

Figure 4(a) shows the variation of the normalized EPWP profiles with normalized depth at a fixed horizontal distance, $x = 4$ m, at various times of the year. Figure 4(b) shows the variation of normalized EPWP with normalized horizontal distance at a fixed depth of $z = 4$ m at various times of the year. For any time instant, Figure 4(a) shows that the EPWP achieves a maximum value at the bottom boundary, owing to the fact that the bottom boundary is non-permeating, thereby preventing water from flowing out and leading to the accumulation of pore pressure at this location. Conversely, the EPWP profiles show zero values at the top boundary, which is permeating and allows the water to drain freely. Figure 4(b) exhibits that at any instant, the maximum EPWP is attained at the non-permeating left boundary, whereas it becomes zero EPWP values at the permeating right boundary.

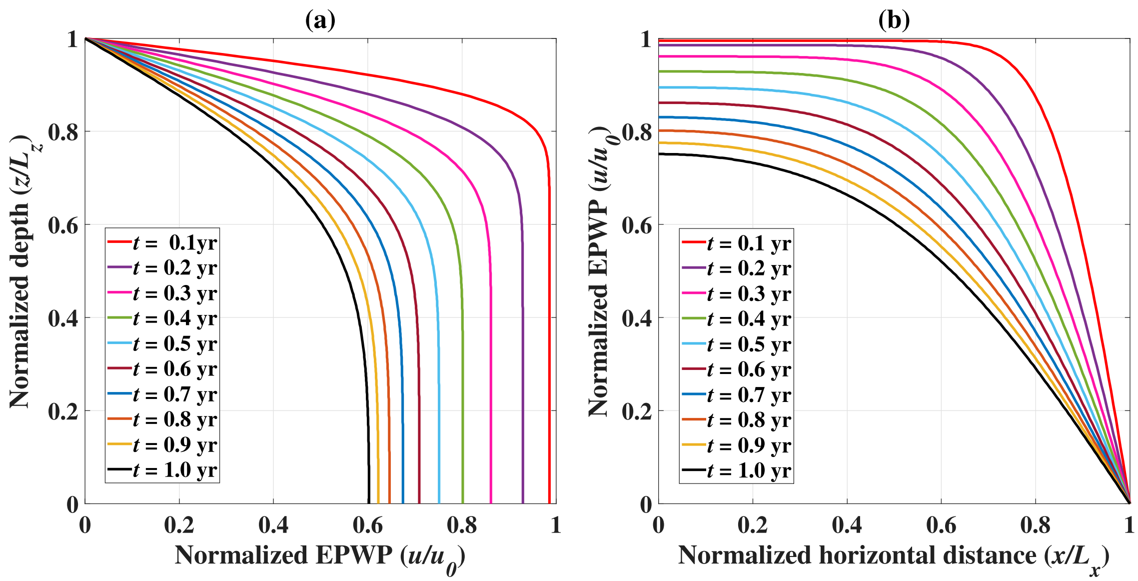

Figure 4: Variation of EPWP profiles with (a) normalized depth and (b) normalized horizontal distance under $S_v S_h$ drainage conditions obtained using the proposed RF-K framework.

The EPWP profiles at a particular time are expected to vary in depth and horizontal distances within the domain. Figure 5 illustrates the shift in the EPWP profile at a specific time of $t = 1.0$ yr across various depths and horizontal distances. In Figure 5(a), the EPWP profile at $t = 1.0$ yr shows a transition from the maximum EPWP value at $x = 0.1$ m to the minimum value as the horizontal distance increases up to $x = 5.9$ m, ultimately reaching zero at $x = 6$ m. Similarly, in Figure 5(b), the EPWP profile at $t = 1.0$ yr shifts from the highest value at $z = 0.1$ m to the minimum value as the depth increases to $z = 5.9$ m, with the EPWP reaching zero at $z = 6.0$ m.

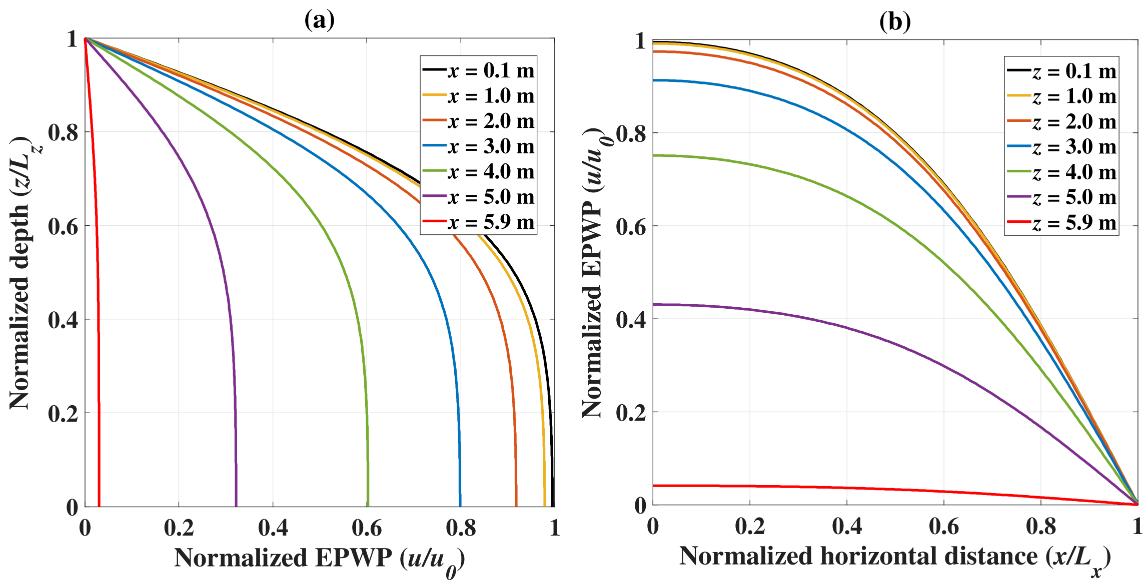

Figure 5: Variation of EPWP profile at t = 1.0 yr (a) with normalized depth at various instants of horizontal distance and (b) with normalized horizontal distance at various instants of depth under S_vS_h drainage conditions.

Figure 6 depicts the temporal variation of EPWP at various depths and horizontal distances. In Figure 6(a), the EPWP varies with time at various depths for a fixed horizontal distance of x = 4 m, while Figure 6(b) shows the EPWP variation with time at various horizontal distances and a fixed depth of z = 4 m. Initially, the EPWP reaches its maximum value; however, as time progresses, the EPWP dissipates rapidly at greater depths and horizontal distances. Near the non-permeating bottom and left boundaries (z = 0 m and x = 0 m), the EPWP dissipates slowly, while it dissipates more quickly near the permeating top and right boundaries (z = 6 m and x = 6 m). In Figure 6(a), EPWP profiles near the non-permeating bottom boundary (up to z = 2.1 m) overlap, indicating minimal variation in EPWP dissipation at these depths. Beyond z = 2.1 m, the profiles diverge significantly, demonstrating increased variation over time. However, in Figure 6(b), EPWP profiles near the non-permeating left boundary exhibit noticeable changes beyond x = 0.9 m.

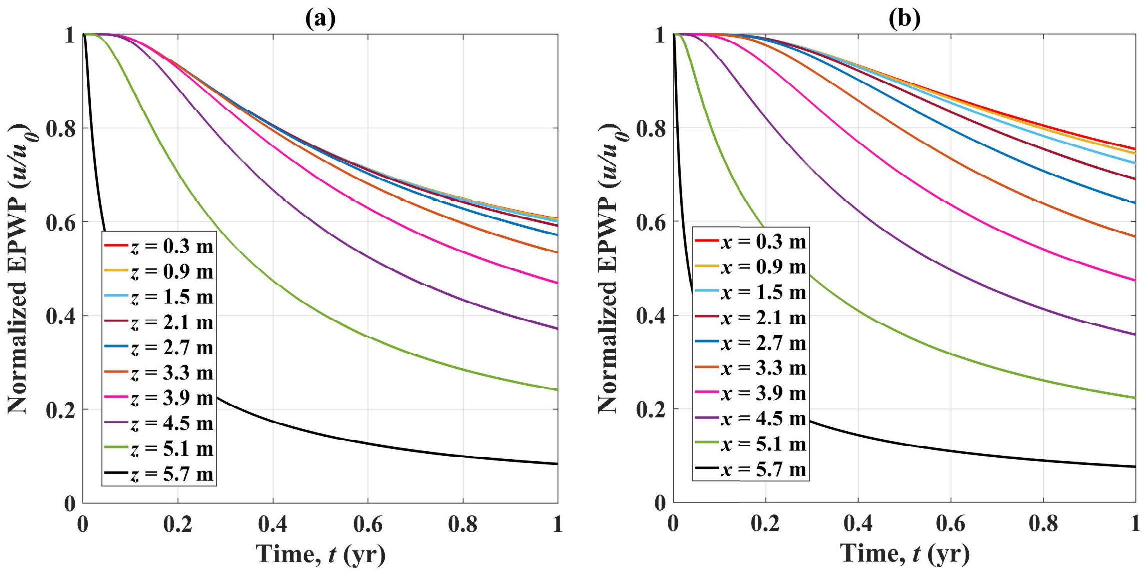

Figure 6: Variation of EPWP profiles with time at various instants of (a) depth at fixed $x = 4$ m and (b) horizontal distance at fixed $z = 4$ m obtained using the proposed RF-K framework under S_vS_h drainage conditions.

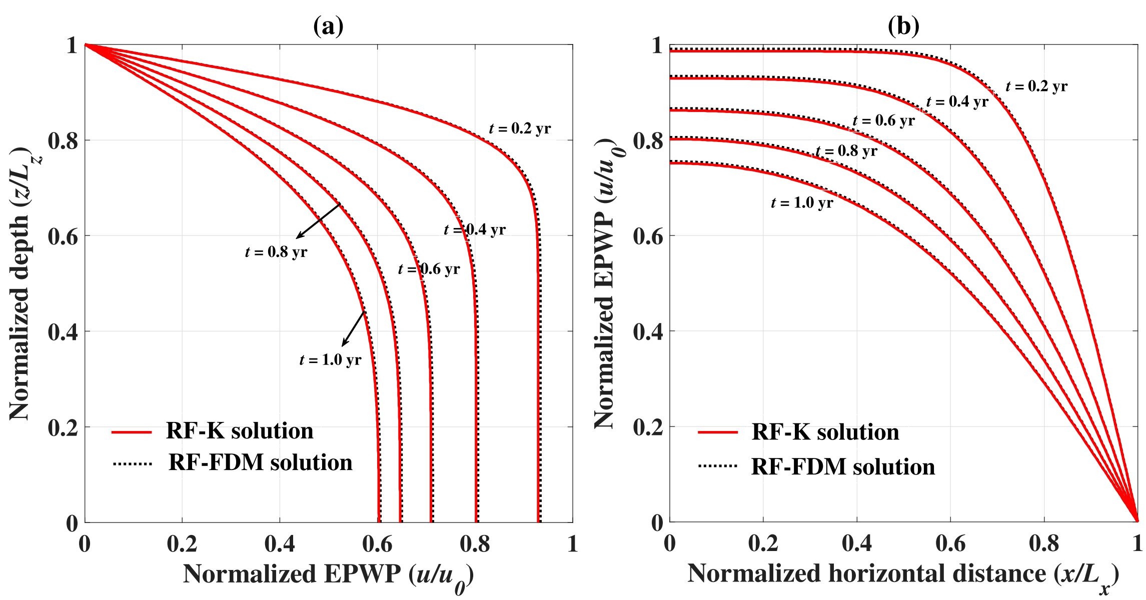

Figure 7: Comparison of RF-K and RF-FDM solutions under S_vS_h drainage showing the variation of EPWP with (a) normalized depth and (b) normalized horizontal distance.

The EPWP solutions derived from the proposed RF-K framework under $S_v S_h$ drainage conditions are compared with those obtained using the RF-FDM framework, ensuring consistent random fields for c_h and c_v, as well as identical domain parameters. Figure 7 presents this comparison, showing the variation of EPWP profiles with normalized depth and normalized distance. The solid red lines correspond to the RF-K solutions, while the black dotted lines represent the RF-FDM solutions. The close alignment between the two sets of results demonstrates excellent agreement, validating the accuracy of the proposed RF-K framework.

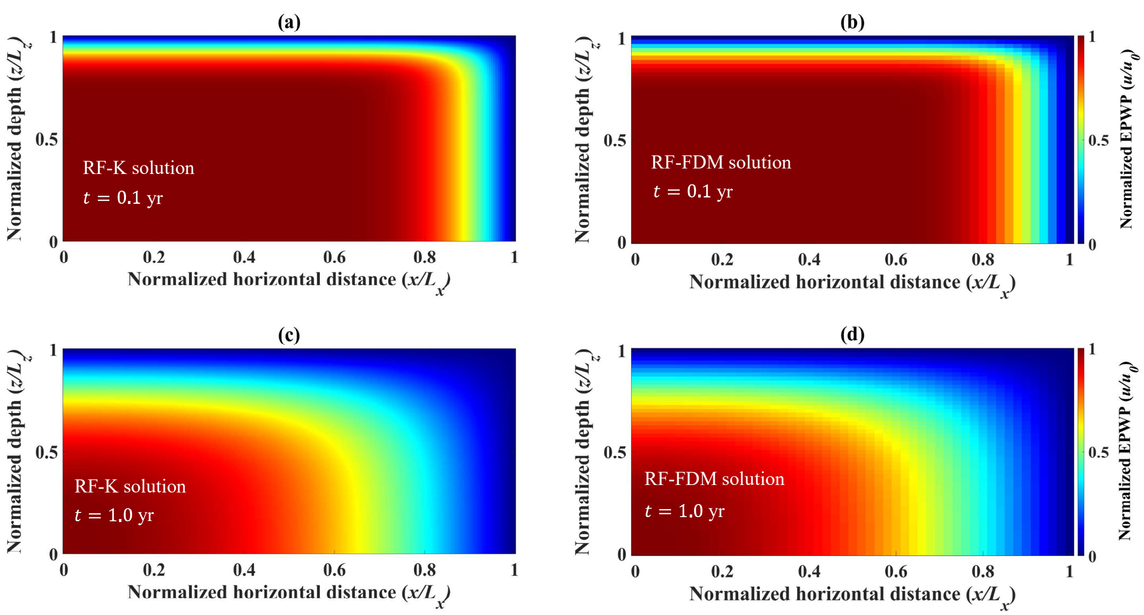

Figure 8: 2D colormaps of EPWP obtained by (a) RF-K at t = 0.5 yr (b) RF-FDM at t = 0.5 yr (c) RF-K at t = 0.9 yr (d) RF-FDM at t = 0.9 yr under $S_v S_h$ drainage boundary conditions.

Figure 8 compares the EPWP colormaps computed using the RF-K and RF-FDM frameworks at $t = 0.1$ yr and $t = 0.1$ yr. These colormaps provide a detailed visualization of the EPWP dissipation as time progresses. Figures 8(a) and 8(b) show the EPWP distribution at $t = 0.1$ yr for RF-K and RF-FDM, respectively. Despite the relatively coarse mesh satisfying the stability criteria, the RF-FDM solution exhibits spatial patterns similar to those observed in the RF-K colormap. At t=1.0 yr, Figures 8(c) and 8(d) display the RF-K and RF-FDM solutions, respectively, demonstrating a close resemblance of the spatial patterns. Notably, the areas near the top and right boundaries, which are permeating, show a rapid decrease in EPWP. In contrast, the EPWP near the lower-left corner remains nearly unchanged, as it is situated far from the drainage boundaries. The mean squared error (MSE) between the two solutions is 9.65×10^{-6}, and the root mean squared error (RMSE) is 0.0031. These results underscore the effectiveness of the RF-K framework in accurately approximating the solution to the 2D consolidation problem as governed by Eq. (4).

5.2 Case 2: 2D Consolidation under $D_v S_h$ Drainage

Under the $D_v S_h$ drainage boundary conditions specified in Eq. (9) and Eq. (10), EPWP solutions for the plane-strain 2D consolidation Eq. (as per (4)), are computed using the proposed RF-K framework. Random fields for c_h and c_v are generated using the Karhunen-Loève (K-L) expansion, with correlation distances of $l_h = 3$ and $l_v = 2$ in the covariance function, consistent with the $S_v S_h$ drainage case. These fields are scaled to the desired ranges of $1.5 - 6\,\mathrm{m}^2/\mathrm{yr}$ for c_h and $0.5 - 2\,\mathrm{m}^2/\mathrm{yr}$ for c_v using Eq. (25) and Eq. (26) respectively. Using a computational domain of $z = 6\,\mathrm{m}$, $x = 6\,\mathrm{m}$, and a time period of $t = 1\,\mathrm{yr}$, EPWP solutions are obtained with the RF-K framework, employing 1000 MCS to simulate the EPWP trajectories. Figure 9 illustrates the variation in EPWP profiles derived from the RF-K framework, with normalized depth at $x = 4$ m, and normalized horizontal distance at $z = 4$ m.

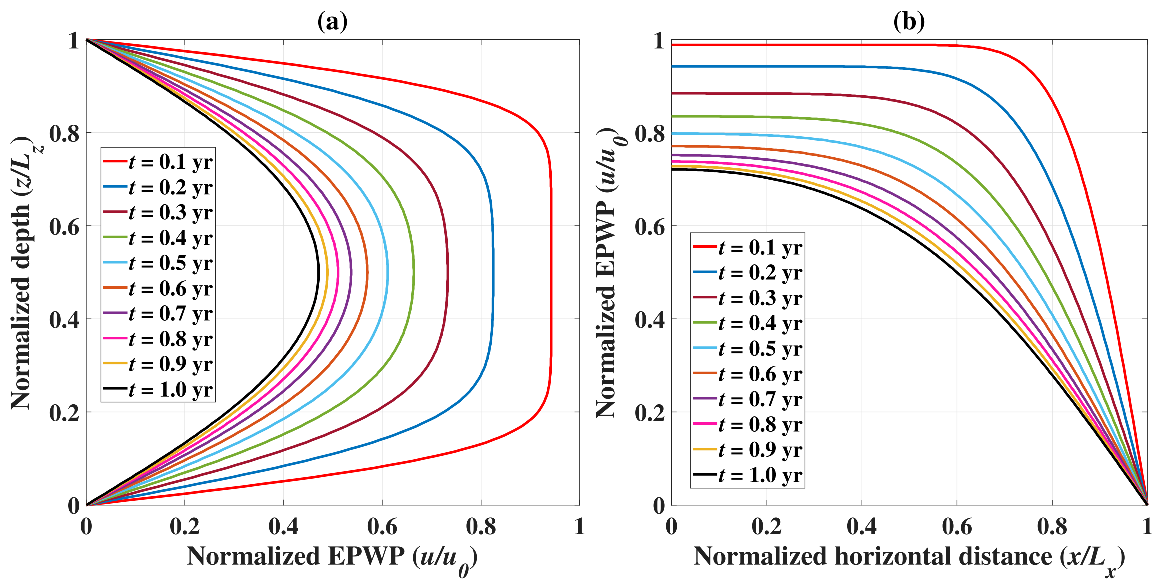

Figure 9: Variation of EPWP profiles with (a) normalized depth and (b) normalized horizontal distance under D_vS_h drainage conditions obtained using the proposed RF-K framework.

The EPWP profiles at each instant show zero values at the top and bottom boundaries and a maximum value at the mid-depth, as shown in Figure 9(a). The EPWP dissipates quickly close to the permeating top and bottom boundaries, while due to a relatively larger distance from the drainage boundaries, the EPWP accumulates to its maximum value at the mid-depth. On a horizontal section, as shown in Figure 9(b), the EPWP attains its maximum at the non-permeating left boundary and progressively decreases to zero at the permeating right boundary.

The transition from the boundary conditions of S_vS_h to D_vS_h, achieved by making the bottom boundary permeating, is evident in the variation of the EPWP profile with depth, as shown in Figure 9(a). However, as shown in Figure 9(b), the pattern of EPWP variation with horizontal distance remains unchanged due to consistent boundary conditions in the horizontal direction, similar to the S_vS_h. Nevertheless, the EPWP values change due to the influence of the permeating top, bottom, and right boundaries, and the non-permeating left boundary, as illustrated in Figure 10. The EPWP values up to t = 0.2 yr remain the same as those in the S_vS_h condition, but beyond t = 0.2 yr, the EPWP profile demonstrates significant increased values for D_vS_h, reaching a maximum variation of 16.5 % at the final consolidation time of t = 1.0 yr. This indicates that rendering the bottom boundary permeating primarily affects the EPWP values rather than the dissipation pattern as observed in the variation with horizontal distance.

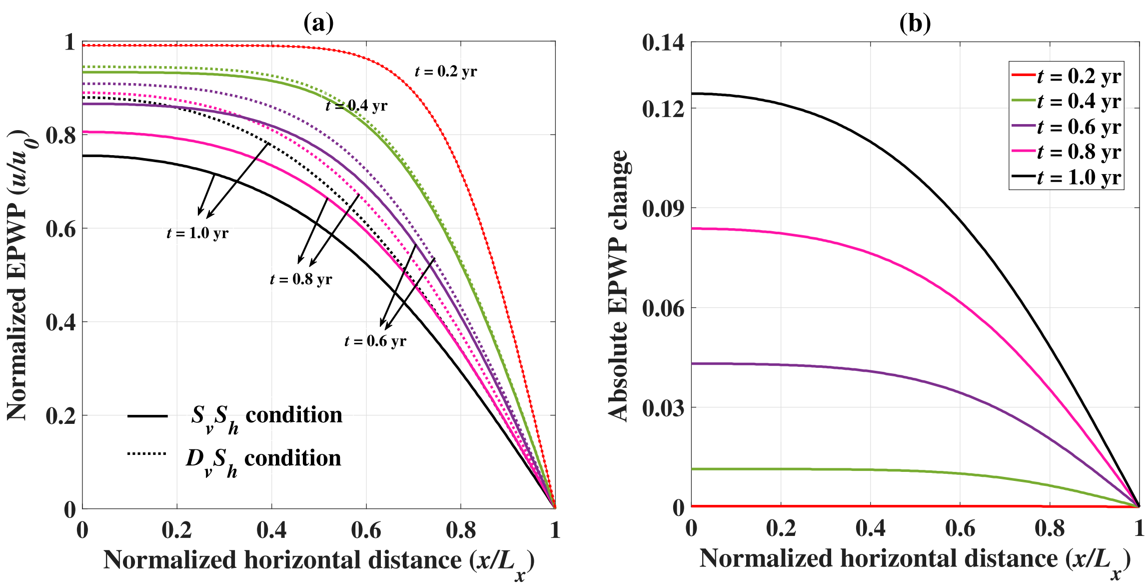

Figure 10: (a) Comparison of the EPWP profile with horizontal distance in S_vS_h and D_vS_h conditions (b) Variation of the change in EPWP values with horizontal distance.

The EPWP profiles for every time instant change with depth and horizontal distance. Figure 11 depicts the reduction in EPWP values as both depth and horizontal distance increase for a specific profile at t = 1.0 yr. Near the non-permeating left boundary, the EPWP values are at their maximum. However, as the horizontal distance approaches the permeating right boundary (x = 6 m), the EPWP values decrease, eventually reaching zero. Figure 11(b) illustrates the variation of

EPWP profiles with horizontal distance at various depths. Understandably, the EPWP profiles are identical to each other symmetrically around the mid-height of the domain (e.g., z = 5.9 m and z = 0.1 m, and so on).

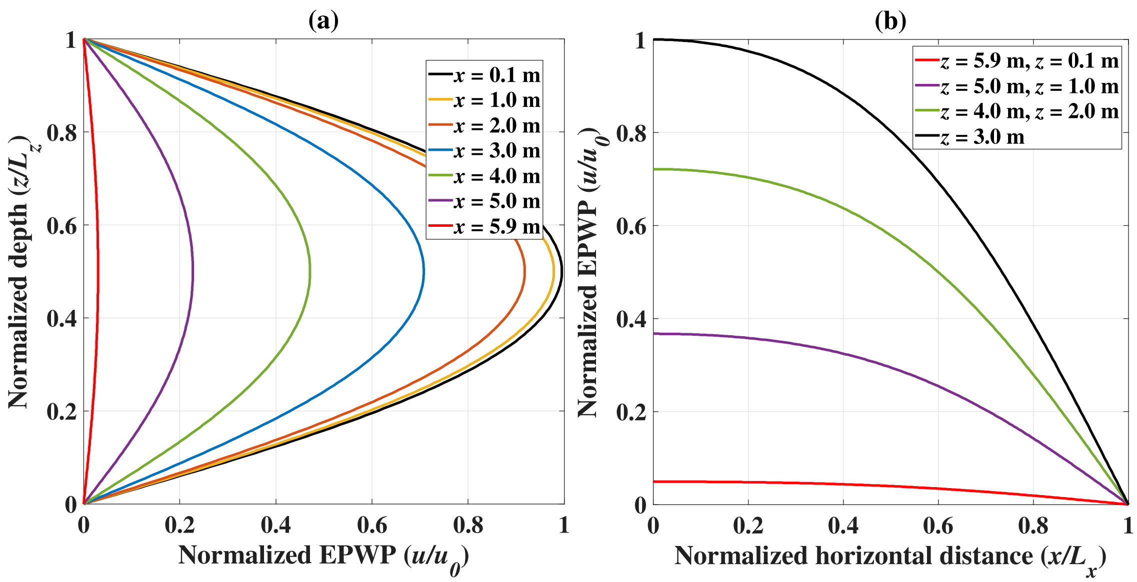

Figure 11: Variation of EPWP profile at t = 1.0 yr (a) with normalized depth at various instants of horizontal distance and (b) with normalized horizontal distance at various instants of depth under $D_v S_h$ drainage conditions.

Figure 12 shows the variation of EPWP with time, exhibiting a faster dissipation near the permeating top, bottom, and right boundaries. Profiles equidistant from the mid-height of the domain (i.e., z = 3, m) overlap with each other. The rate of EPWP dissipation gets progressively slower for profiles towards the mid-depth. For the variation of EPWP with time at different horizontal distances and a fixed depth of z = 4 m, as shown in Figure 12(b), the EPWP near the non-permeating left boundary (x = 0 m to x = 3 m) dissipates gradually, with minimal variation between profiles. Closer to the permeating right boundary (x = 3 m to x = 6 m), the dissipation is more rapid, resulting in notable changes in the profiles due to the influence of the permeating boundary.

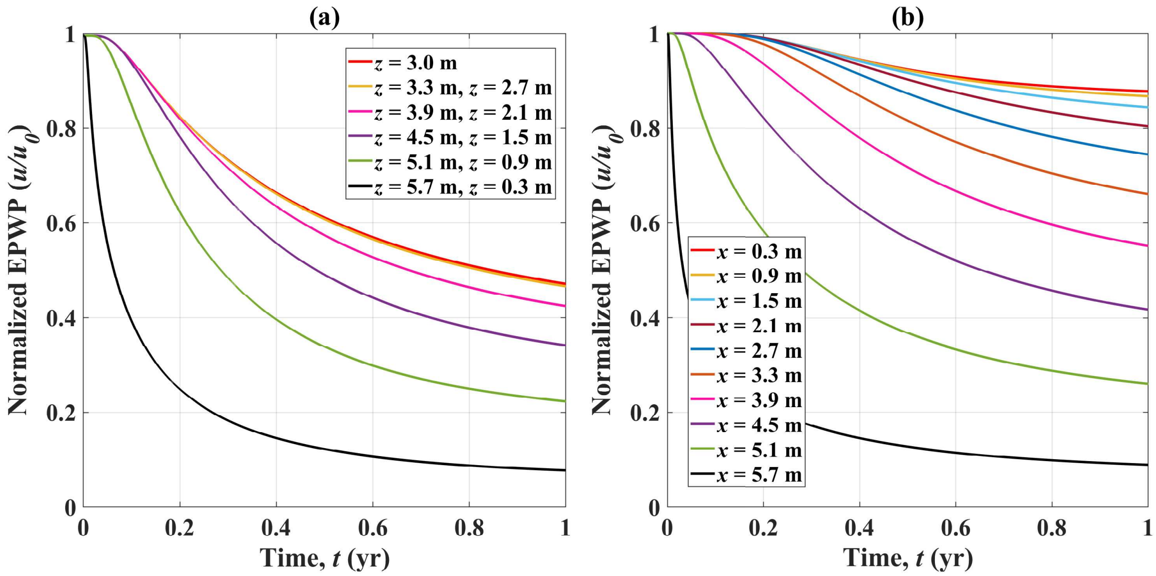

Figure 12: Variation of EPWP profiles with time at various instants of (a) depth at fixed $x = 4$ m and (b) horizontal distance at fixed $z = 4$ m obtained using the proposed RF-K framework under $D_v S_h$ drainage conditions.

The EPWP dissipation profile over time at various horizontal distances in $D_v S_h$ drainage conditions, as in Figure 12(b), exhibits notable differences as compared to $S_v S_h$ case due to the introduction of the permeating bottom boundary. This effect is more pronounced near the non-permeating left boundary ($x = 0$ m), while the variation diminishes towards the permeating right boundary ($x = 6$ m), as illustrated in Figure 13. The maximum EPWP variation of 16.5 % occurs at $x = 0.3$ m, as shown in Figure 13(b). Additionally, the presence of the permeating bottom boundary in the $D_v S_h$ case facilitates rapid EPWP dissipation in the vertical direction. However, it also leads to a slower EPWP dissipation rate in the horizontal direction compared to the $S_v S_h$ case, as shown in Figure 13(a). This occurs because the pore water in the soil domain preferentially drains more from the vertical boundaries, reducing the hydraulic gradient in the horizontal direction, which slows down the EPWP dissipation in the horizontal direction.

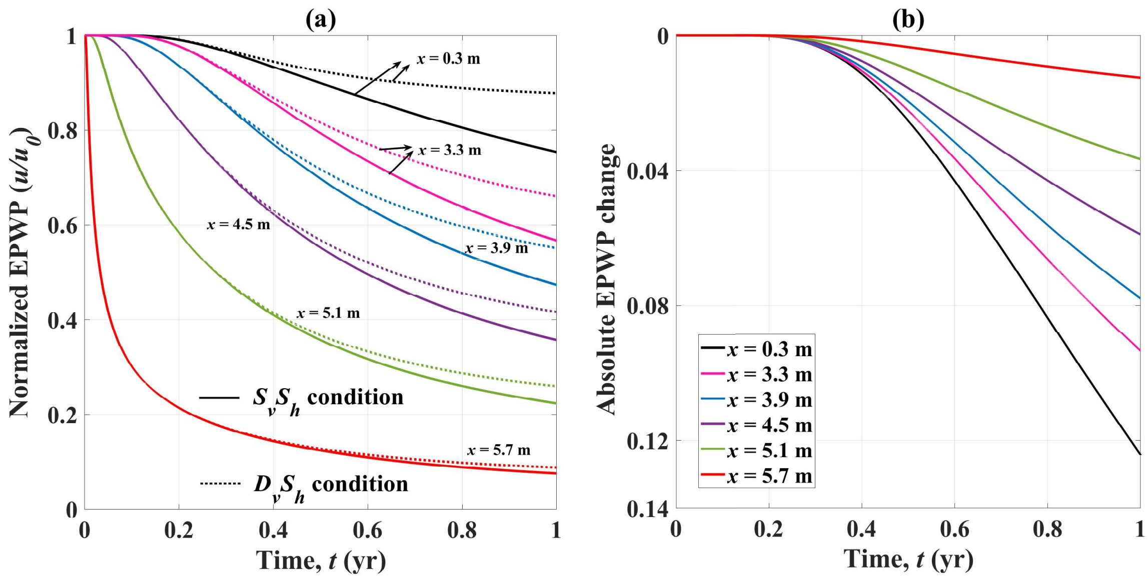

Figure 13: (a) Comparison of the EPWP profile with time in S_vS_h and D_vS_h conditions (b) Variation of the change in EPWP values with time at various horizontal distances.

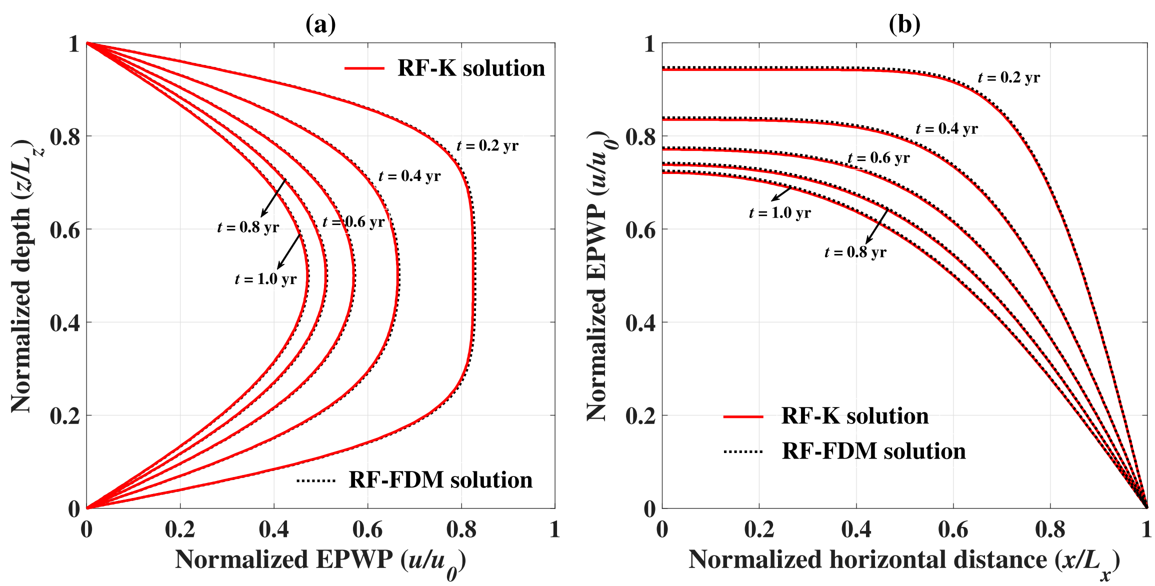

Figure 14: Comparison of RF-K and RF-FDM solutions under D_vS_h drainage showing the variation of EPWP with (a) normalized depth and (b) normalized horizontal distance.

The EPWP profiles computed using the proposed RF-K framework under D_vS_h drainage boundary conditions, as shown in Figure 9, are compared with those obtained using the RF-FDM framework. The comparison employs the same random fields for c_h and c_v and identical domain parameters. Figure 14 illustrates the EPWP profiles from both frameworks at selected time periods, depths, and horizontal distances. The profiles exhibit excellent agreement, validating the accuracy and effectiveness of the RF-K framework in solving the 2D consolidation problem under D_vS_h drainage conditions.

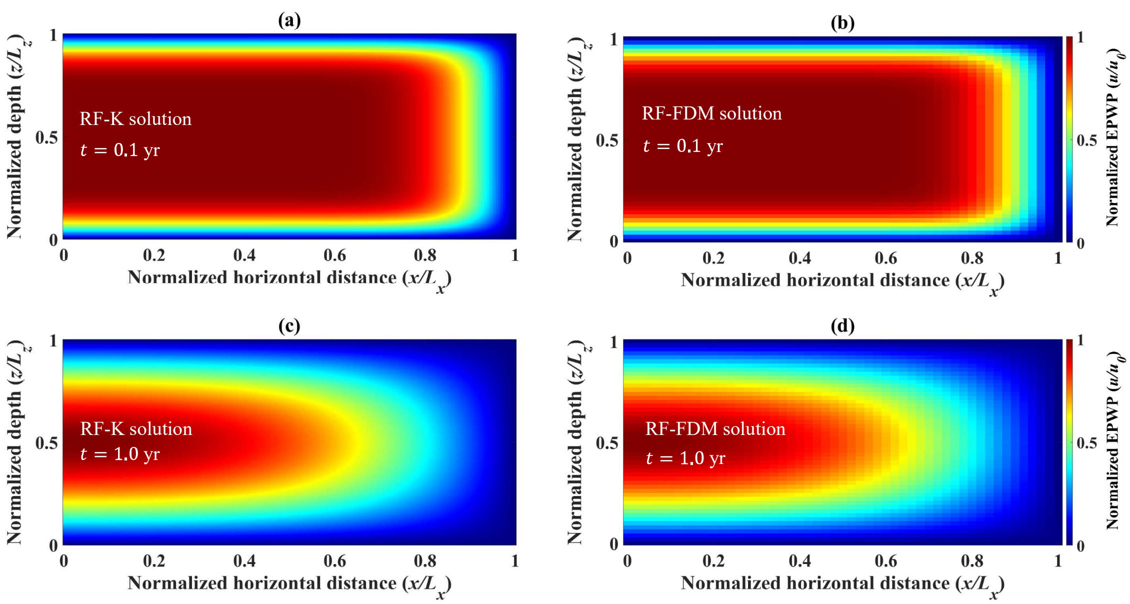

Figure 15: 2D colormaps of EPWP obtained by (a) RF-K at t = 0.5 yr (b) RF-FDM at t = 0.5 yr (c) RF-K at t = 0.9 yr (d) RF-FDM at t = 0.9 yr under D_vS_h drainage conditions.

Figure 15 compares the 2D colormaps of the EPWP computed using the proposed RF-K and RF-FDM frameworks at t = 0.1 yr and t = 1.0 yr under D_vS_h drainage conditions. The colormaps reveal that even after one year of consolidation, the maximum EPWP persists near the mid-depth, close to the non-permeating left boundary of the domain. The effect of intersecting permeating boundaries (top and bottom right corners) is nicely captured by the changing shape of the EPWP colormaps, which transition from a more rectangular to an elliptical behavior (losing corner prominence) with progressing consolidation. The RF-FDM colormaps align closely with the spatial patterns of the EPWP profiles obtained from the RF-K framework at both time instances. The MSE between the two solutions is 7.29×10^{-6}, and the RMSE is 0.0027.

However, the computational cost of RF-FDM is significantly higher than the proposed RF-K approach. For a spatial domain of 6 m × 6 m, a time duration of 1 yr, and a spatial discretization of 200 × 200, the RF-FDM approach requires approximately 6550.15 seconds, whereas the RF-K framework requires only 2352.29 seconds, achieving a 64% reduction in computation time. Furthermore, using parallel computing reduces the computation time of the RF-K framework to 1853.6 seconds, achieving a 71.7% reduction, making it 3.53 times faster than the RF-FDM framework. These results demonstrate the computational efficiency and capability of the R-FK framework to accurately capture the solution to the 2D consolidation problem governed by Eq. (4).

In addition to the computational efficiency, the proposed RF-K framework is also meshless. Unlike RF-FDM, which relies on a specified grid structure satisfying the time-step criteria as outlined in Eq. (24), the proposed RF-K framework does not require a predefined grid structure to compute stable solutions of the 2D consolidation problem. For a spatial discretization of 100×100, $\Delta x = 0.01$, $\Delta z = 0.01$, and c_h and c_v modeled as random fields in the range of 1.5–6.0 m^2/yr and 0.5–2.0 m^2/yr, respectively, a time step of $\Delta t = 0.01$ leads to unstable EPWP profiles in the RF-FDM framework due to the violation of the stability criteria. In contrast, the proposed RF-K framework remains stable and produces accurate solutions, demonstrating its robustness in solving the 2D consolidation problem without being constrained by strict stability conditions.

5.3 Application to 1D consolidation: Case Study

To further validate its robustness and applicability, the proposed RF-K framework is applied to the 1D consolidation of saturated soils. This 1D case represents a dimensionally degenerated version of the 2D consolidation problem. By imposing non-permeating conditions on the left and right boundaries of the 2D soil domain, horizontal dissipation pore water is restricted, allowing vertical drainage only through the top permeating boundary. This modification effectively reduces the problem to a 1D scenario. For the 1D consolidation problem, the RF-FDM scheme of Eq. (27) reduces to

$$u_i^{n+1} = u_i^n + \Delta t\left[\left\{\overline{c_v(z)} + \sum_{k=1}^{N} \sqrt{\lambda_{v_k}}\psi_k(z)\eta_k(\omega)\right\}\frac{u_{i+1}^n - 2u_i^n + u_{i-1}^n}{\Delta z^2}\right] \tag{48}$$

For the 1D case, only the coefficient of vertical consolidation, c_v, is modeled as a 1D random field to incorporate the spatial variability. For the RF-K framework, the EPWP solution given by Eq. (38) reduces for the 1D case, given by

$$u(z,t) = E_\eta\left[E[\zeta(z(T_e)) \mid Z_t = z]\right] \tag{49}$$

The solution of EPWP using the RF-K framework is obtained by simulating the SDE given by Eq. (31), subjected to the initial boundary conditions as in Eq. (2), and considering a random field of c_v. A depth of $z = 2$ m and a time of $t = 1$ yr are considered, and a random field of c_v is generated in the range of 0.5 – 2 m^2/yr to obtain the RF-K solution of the 1D consolidation problem.

Figure 16 illustrates the EPWP solution for 1D consolidation using the RF-K framework. In Figure 16(a), EPWP profiles are shown varying with normalized depth at different time intervals, with maximum EPWP at the impermeating bottom boundary and zero EPWP at the permeating top boundary. The profiles also indicate a progressive reduction in EPWP over time due to dissipation. Figure 16(b) presents a colormap of the EPWP solution, highlighting rapid dissipation near the permeating top boundary, while significant EPWP remains entrapped at the non-permeating bottom boundary.

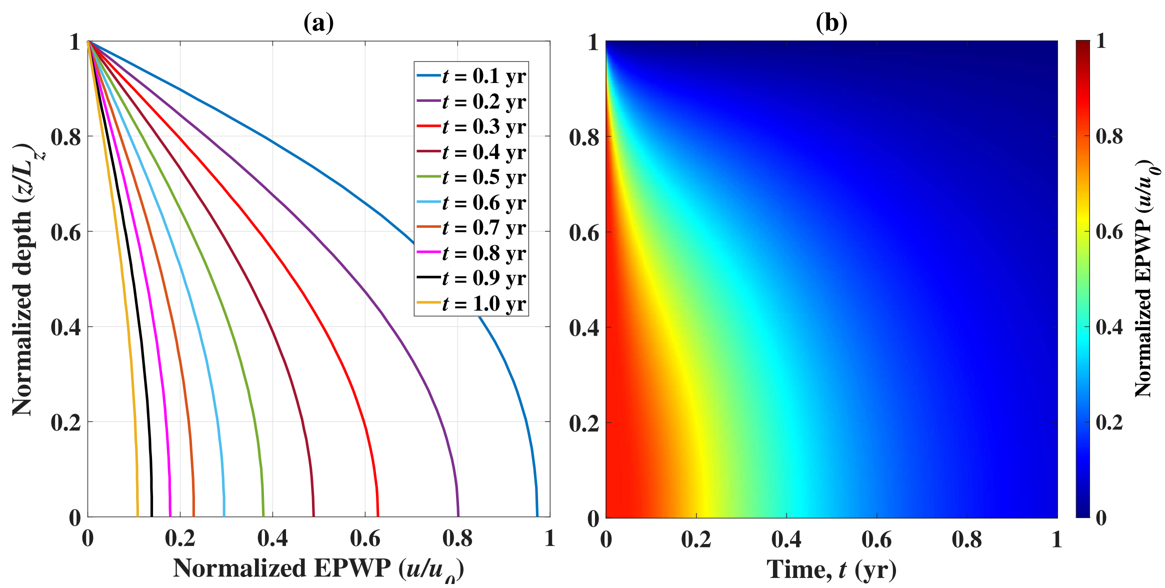

Figure 16: 1D consolidation solution showing (a) variation of normalized EPWP with normalized depth and (b) 2D colormap of EPWP obtained using the proposed RF-K framework under S_v drainage condition.

The RF-FDM solution of the 1D consolidation Eq. (1) is computed by solving Eq. (48) for each time step, considering the same random field of c_v. The analytical solution of the 1D consolidation Eq. (1) is obtained using Eq. (3) for the same depth and time parameter values. To assess the accuracy of the proposed RF-K framework, the EPWP solutions obtained from the RF-K approach are compared with both the analytical (Figure 17(a)) and RF-FDM (Figure 17(b)) solutions. In both cases, the EPWP profiles exhibit excellent agreement across the methods. The MSE between the analytical and RF-K solutions is 3.11×10^{-6}, while the MSE between the RF-

FDM and RF-K solutions is 1.99×10^{-6}. Similarly, the RMSE values are 0.0018 for the analytical and RF-K comparison and 0.0014 for the RF-FDM and RF-K comparison, further confirming the accuracy of the RF-K framework.

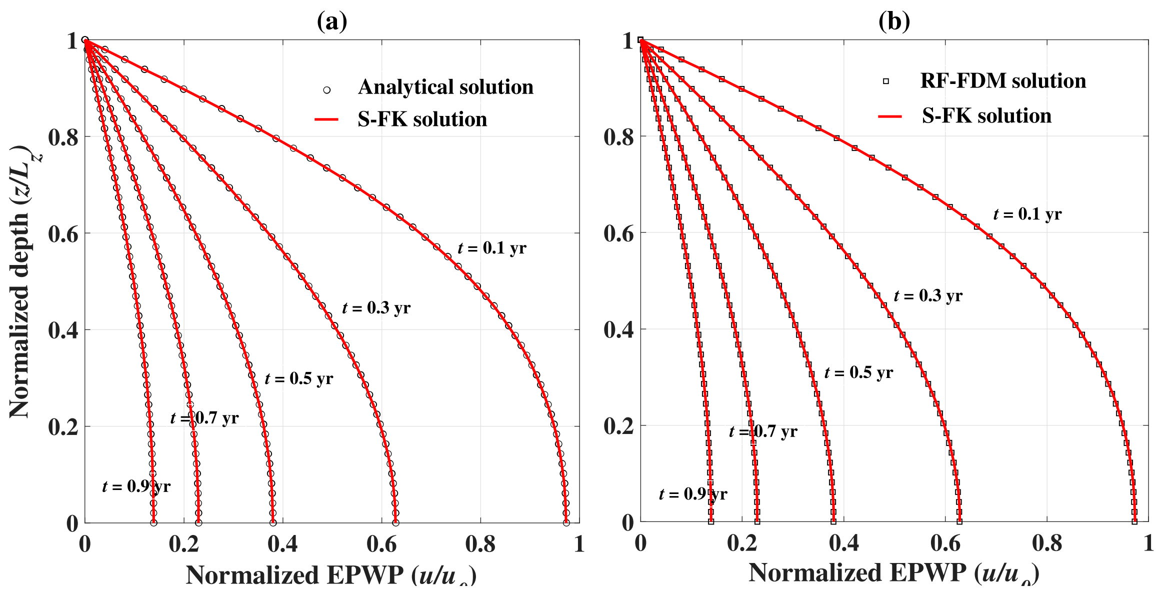

Figure 17: Comparison of the EPWP profiles obtained using the RF-K solution with the (a) analytical solution and (b) RF-FDM solution for the 1D consolidation problem.

6 CONCLUSIONS

In the present study, a novel and robust stochastic framework is developed for solving the plane-strain 2D consolidation of saturated soils. The framework employs the Feynman-Kac formula and the Karhunen-Loeve expansion technique to address the spatial variability of soils. Specifically, the coefficients of horizontal and vertical consolidation, c_h and c_v, are modeled as random fields using K-L expansion. The proposed RF-K framework solves the 2D consolidation PDE by generating corresponding SDEs and simulating them until the exit time using MC simulations under various cases of S_vS_h and D_vS_h drainage boundary conditions. The boundary conditions are handled uniquely in the framework as reflective or absorbent boundaries, and the Brownian particles are either reflected back or allowed to escape the domain according to the boundary conditions. By simulating the trajectories of the Brownian particles until they reach the domain boundaries, the framework constructs the excess pore water pressure (EPWP) field as an ensemble average over these trajectories. This approach provides a probabilistic solution to the 2D consolidation PDE while incorporating soil heterogeneity and boundary effects in a computationally efficient manner.

In addition, a numerical framework employing the finite difference incorporating the random fields of c_h and c_v is also developed to obtain solutions to the 2D consolidation. This RF-FDM framework models the coefficients of horizontal and vertical consolidation, c_h and c_v, as random fields, similar to the proposed RF-K framework. The RF-FDM framework provides EPWP solutions to the 2D consolidation problem subjected to various cases of S_vS_h and D_vS_h drainage boundary conditions. The EPWP solutions obtained from the proposed RF-K framework are compared with those derived from the RF-FDM framework employing the same fields of c_h and c_v. The results demonstrate excellent agreement between the two approaches across all boundary conditions, as indicated by low MSE and RMSE values. This highlights the robustness of the RF-K framework in accurately handling the spatial variability of soils and addressing various drainage boundary cases of the 2D consolidation phenomenon.

Furthermore, the proposed RF-K framework is applied to the simple case of the 1D consolidation problem under S_v drainage boundary conditions, allowing water to be drained only in the vertical direction. This application serves to validate the accuracy and versatility of the proposed framework in the light of both analytical and RF-FDM solutions. The results demonstrate excellent agreement among the methods, as evidenced by even lower values of MSE and RMSE for the 1D case. The developed RF-K framework proves to be a robust and meshless approach for solving both 2D and 1D consolidation problems of soft soils, effectively incorporating spatial variability and addressing various drainage boundary conditions.

Data Availability Statement

Some or all data, models, or code that support the findings of this study are available from the corresponding author upon reasonable request.

Declaration of conflicting interests

The author(s) declared no potential conflicts of interest with respect to the research, authorship, and/or publication of this article.

REFERENCES

[1] K. Terzaghi, Principles of soil mechanics, IV—Settlement and consolidation of clay, Eng. News-Rec. 95 (3) (1925) 874–878.

[2] L. Rendulic, Porenziffer und porenwasserdruck in tonen, Der Bauingenieur 17 (1936) 559–564.

[3] T. Elkateb, R. Chalaturnyk, P. K. Robertson, An overview of soil heterogeneity: quantification and implications on geotechnical field problems, Can. Geotech. J. 40 (1) (2003) 1–15. doi:10.1139/t02-090.

[4] C. S. Chang, Uncertainty of one-dimensional consolidation analysis, J. of Geotech. Eng., ASCE 111 (12) (1985) 1411–1424. doi:10.1061/(ASCE)0733-9410(1985)111:12(1411).

[5] K.-K. Phoon, F. H. Kulhawy, Characterization of geotechnical variability, Can. Geotech. J. 36 (4) (1999) 612–624. doi:10.1139/t99-038.

[6] S. E. Cho, Effects of spatial variability of soil properties on slope stability, Eng. Geol. 92 (3-4) (2007) 97–109.

doi:10.1016/j.enggeo.2007.03.006.

[7] D. J. Mulla, A. B. McBratney, Soil Physics Companion, CRC Press, Boca Raton, 2001, Ch. Soil spatial variability, pp. 343–373. doi:10.1201/9781420041651.

[8] S. Valliappan, J. T. Yazdi, C. Zhao, Analytical solution for two-dimensional dynamic consolidation in frequency domain, Int. J. Numer. Anal. Methods Geomech. 19 (10) (1995) 663–682. doi:10.1002/nag.1610191002.

[9] A. Qin, D. Sun, L. Yang, Y. Weng, A semi-analytical solution to consolidation of unsaturated soils with the free drainage well, Comput. Geotech. 37 (7-8) (2010) 867–875. doi:10.1016/j.compgeo.2010.07.006.

[10] L. Ho, B. Fatahi, Analytical solution for the two-dimensional plane strain consolidation of an unsaturated soil stratum subjected to time-dependent loading, Comput. Geotech. 67 (2015) 1–16. doi:10.1016/j.compgeo.2015.02.011.

[11] Y. Liu, J.-J. Zheng, L. You, J.-T. Lu, L. Cui, W.-Y. Yang, Z.-F. Huang, An Analytical Solution for 2D Plane Strain Consolidation in Unsaturated Soils with Lateral and Vertical Semipermeable Drainage Boundaries under Time-Dependent Loading, Int. J. Geomech. 22 (12) (2022) 06022032. doi:10.1061/(ASCE)GM.1943-5622.0002508.

[12] M. Huang, J. Li, Generalized analytical solution for 2D plane strain consolidation of unsaturated soil with time-dependent drainage boundaries, Comput. Geotech. 103 (2018) 218–228. doi:10.1016/j.compgeo.2018.07.012.

[13] L. Wang, S. Shen, T. Li, M. Wen, A. Zhou, Two-dimensional plane strain consolidation of unsaturated soils considering the depth-dependent stress, J. Rock Mech. Geotech. Eng. 15 (6) (2023) 1603–1614. doi:10.1016/j.jrmge.2022.08.011.

[14] S.-L. Xie, A.-F. Hu, Z.-R. Xiao, M.-H. Wang, X.-J. Hu, G. Della Vecchia, S. Mariani, Analysis of two-dimensional consolidation behavior of soils under cyclic loading considering exacerbated tunnel leakage, Comput. Geotech. 174 (2024) 106637. doi:10.1016/j.compgeo.2024.106637.

[15] C. Sun, T. Yu, B. Liu, H. Wei, F. Tan, Semianalytic Solution for Two-Dimensional Consolidation of Interbedded Soil, Int. J. Geomech. 24 (9) (2024) 04024203. doi:10.1061/IJGNAI.GMENG-9575.

[16] M. Shoji, H. Ohta, K. Arai, T. Matsumoto, T. Takahashi, Two-Dimensional Consolidation Back-Analysis, Soils Found. 30 (2) (1990) 60–78. doi:10.3208/sandf1972.30.2_60.

[17] M. Hassanen, A. El-Hamalawi, Two-dimensional development of the dynamic coupled consolidation scaled boundary finite-element method for fully saturated soils, Soil Dyn. Earthq. Eng. 27 (2) (2007) 153–165. doi:10.1016/j.soildyn.2006.05.003.

[18] M. Baqersad, A. E. Haghighat, M. Rowshanzamir, H. M. Bak, Comparison of Coupled and Uncoupled Consolidation Equations Using Finite Element Method in Plane-Strain Condition, Civ. Eng. J. 2 (8) (2016) 375–388. doi:10.28991/cej-2016-00000042.

[19] Y. Tang, H. A. Taiebat, A. R. Russell, Numerical Modeling of Consolidation of Unsaturated Soils Considering Hydraulic Hysteresis, Int. J. Geomech. 18 (2) (2018) 04017136. doi:10.1061/(ASCE)GM.1943-5622.0001047.

[20] J. Huang, D. Griffiths, G. A. Fenton, Probabilistic Analysis of Coupled Soil Consolidation, J. Geotech. Geoenviron. Eng. 136 (3) (2010) 417–430. doi:10.1061/(ASCE)GT.1943-5606.0000238.

[21] T. Bong, A. W. Stuedlein, Efficient methodology for probabilistic analysis of consolidation considering spatial variability, Eng. Geol. 237 (2018) 53–63. doi:10.1016/j.enggeo.2018.02.009.

[22] T. Bong, Y. Son, S. Noh, J. Park, Probabilistic analysis of consolidation that considers spatial variability using the stochastic response surface method, Soils Found. 54 (5) (2014) 917–926. doi:10.1016/j.sandf.2014.09.005.

[23] Y. Houmadi, M. Y. C. Benmoussa, W. N. E. H. Cherifi, D. D. Rahal, Probabilistic analysis of consolidation problems using subset simulation, Comput. Geotech. 124 (2020) 103612. doi:https://doi.org/10.1016/j.compgeo.2020.103612.

[24] Y. W. Bekele, Physics-informed deep learning for one-dimensional consolidation, J. Rock Mech. Geotech. Eng. 13 (2) (2021) 420–430. doi:10.1016/j.jrmge.2020.09.005.

[25] Y. Lu, G. Mei, A Deep Learning Approach for Predicting Two-Dimensional Soil Consolidation Using Physics-Informed Neural Networks (PINN), Mathematics 10 (16) (2022) 2949. doi:10.3390/math10162949.

[26] S. Xie, A. Hu, Z. Xiao, S. Mariani, G. Della Vecchia, PINN-based approach to the consolidation analysis of

visco-elastic soft soil around twin tunnels, Tunn. Undergr. Space Technol. 153 (2024) 105981. doi:10.1016/j.tust.2024.105981.

[27] Y. Wang, C. Shi, J. Shi, H. Lu, Data-driven forward and inverse analysis of two-dimensional soil consolidation using physics-informed neural network, Acta Geotech. 19 (2024) 8051–8069. doi:10.1007/s11440-024-02345-5.

[28] H. Guo, Z.-Y. Yin, A novel physics-informed deep learning strategy with local time-updating discrete scheme for multi-dimensional forward and inverse consolidation problems, Comput. Methods Appl. Mech. Eng. 421 (2024) 116819. doi:10.1016/j.cma.2024.116819.

[29] L. Bertini, N. Cancrini, The stochastic heat equation: Feynman-Kac formula and intermittence, J. Stat. Phys. 78 (1995) 1377–1401. doi:10.1007/BF02180136.

[30] P. Del Moral, Feynman-Kac Formulae, Springer, New York, 2004. doi:10.1007/978-1-4684-9393-1.

[31] R. P. Feynman, Space-Time Approach to Non-Relativistic Quantum Mechanics, Rev. Mod. Phys. 20 (2) (1948) 367–387. doi:10.1103/RevModPhys.20.367.

[32] Y. Hu, D. Nualart, J. Song, Feynman–Kac formula for heat equation driven by fractional white noise, The Annals of Probability 39 (1) (2011) 291–326. doi:10.1214/10-AOP547.

[33] M. Caffarel, P. Claverie, Development of a pure diffusion quantum Monte Carlo method using a full generalized Feynman–Kac formula. I. Formalism, J. Chem. Phys. 88 (2) (1988) 1088–1099. doi:10.1063/1.454227.

[34] D. Nualart, W. Schoutens, Backward Stochastic Differential Equations and Feynman-Kac Formula for Lévy Processes, with Applications in Finance, Bernoulli 7 (5) (2001) 761–776. doi:10.2307/3318541.

[35] H. Alghassi, A. Deshmukh, N. Ibrahim, N. Robles, S. Woerner, C. Zoufal, A variational quantum algorithm for the Feynman-Kac formula, Quantum 6 (2022) 730. doi:10.22331/q-2022-06-07-730.

[36] K. P. Hawkins, A. Pakniyat, E. Theodorou, P. Tsiotras, Solving Feynman-Kac Forward Backward SDEs Using McKean-Markov Branched Sampling, IEEE Trans. Autom. Control (2024). doi:10.1109/TAC.2023.3349173.

[37] A. Verruijt, Theory and problems of poroelasticity, Delft University of Technology 71 (2013) 465.

[38] T. W. Lambe, R. V. Whitman, Soil Mechanics, Vol. 10, John Wiley & Sons, 1991.

[39] S. Särkkä, A. Solin, Applied Stochastic Differential Equations, Vol. 10, Cambridge University Press, 2019.

[40] G. A. Fenton, D. V. Griffiths, et al., Risk Assessment in Geotechnical Engineering, Vol. 461, John Wiley & Sons, 2008. doi:10.1002/9780470284704.

[41] I. C. Tsantili, D. T. Hristopulos, Karhunen–Loève expansion of Spartan Spatial Random Fields, Probabilistic Eng. Mech. 43 (2016) 132–147. doi:10.1016/j.probengmech.2015.12.002.

[42] G. J. Lord, C. E. Powell, T. Shardlow, An Introduction to Computational Stochastic PDEs, Vol. 50, Cambridge University Press, 2014. doi:10.1017/CBO9781139017329.

[43] K.-K. Phoon, Reliability-based design of foundations for transmission line structures, Cornell University, 1995. doi:10.1016/S0266-352X(99)00037-3.

[44] J. Chu, M. W. Bo, M. Chang, V. Choa, Consolidation and Permeability Properties of Singapore Marine Clay, J. Geotech. Geoenviron. Eng. 128 (9) (2002) 724–732. doi:10.1061/(ASCE)1090-0241(2002)128:9(724).